AN ANALYSIS OF LAMELLAR X-RAY DIFFRACTION FROM DISORDERED MEMBRANE MULTILAYERS WITH APPLICATION TO DATA FROM RETINAL ROD OUTER SEGMENTS

STEPHEN SCHWARTZ, JAMES E. CAIN, EDWARD A. DRATZ, *and* J. KENT BLASIE

From the Division of Natural Sciences, University of California, Santa Cruz, California 95064, and Johnson Research Foundation, University of Pennsylvania, Philadelphia, Pennsylvania 19174. Dr. Cain's present address is the Biology Department, Brookhaven National Laboratory, Upton, New York 11973.

ABSTRACT Oriented multilayers containing a membrane pair within the unit cell potentially possess both lattice disorder and substitution disorder. Lattice disorder occurs when there is a lack of long-range order in the lattice spacings produced by a variation in the nearest neighbor distances between unit cells. A simple form of substitution disorder can arise from a variation in the separation of the two membranes within the unit cells in the multilayer. Lattice disorder produces a monotonically increasing width for higher order lamellar "reflections" while simple substitution disorder produces an incoherent intensity underlying the coherent intensity. A generalized Patterson function analysis has been developed for treating lamellar diffraction from lattice disordered multilayers. This analysis allows the identification of the autocorrelation function of the unit cell electron density profile and its subsequent deconvolution to provide the unit cell electron density profile. A recursive procedure has been developed for separating the incoherent intensity from the coherent intensity via a Gaussian probability model of the membrane intra-pair separation. In cases studied so far both disorders can be quantitatively accounted for and eliminated from interfering with the phasing of the coherent intensity or distorting the derived electron density profile. Lamellar X-ray diffraction data from intact retinal rods, using either film or position sensitive detectors, shows severe effects of both forms of disorder which have not been taken into account in past analysis of such data. We have applied our analysis to the data on dark adapted rod outer segments in electrophysiologically intact retinas of Chabre and Cavaggioni (unpublished). An electron density profile is derived at 25 Å resolution. The lattice nearest neighbor spacing has a variation of ±19 Å out of a 295 Å repeat. The intra-unit cell membrane pair center to center distance of 88 Å varies ±8 Å.

INTRODUCTION

Oriented multilayers of natural and artificial membranes present an appropriate material for structural analysis by X-ray diffraction. Several reviews exist on this subject (Shipley, 1973; Levine, 1973; Worthington, 1973*a*; Luzzati, 1968). One such naturally

occurring multilayer system is the retinal rod outer segment, which consists of a stack of about 1,000 flattened vesicular disks. Biomembrane vesicles can also be prepared as an oriented multilayer by appropriate pelleting in the ultracentrifuge. Retinal rod outer segment disk membranes (Santillan and Blasie, in preparation), photosynthetic bacterial chromatophore membranes (Cain, 1974 *a*, *b*; Cain and Blasie, in preparation), and sarcoplasmic reticulum membranes (Marquardt and Blasie, in preparation; Dupont et al., 1973; Worthington and Liu, 1973) are being studied by this method. Other methods have been used to prepare fatty acid (Lesslauer and Blasie, 1972) and phospholipid bilayers (Lesslauer et al., 1971; Levine and Wilkins, 1971) as oriented multilayers for X-ray diffraction analysis.

The ultimate goal of the X-ray analyses is to determine the molecular structure and arrangement in these artificial and natural membranes. When properly analyzed, the lamellar diffraction (the diffraction along a line normal to the plane of the multilayer) yields the electron density profile of a single layer or unit cell. The electron density profile is the projection of the electron density of the multilayer onto a line normal to the layer plane. Interpretation of the molecular arrangement within the cross section of these membranes in terms of the disposition of lipid and protein requires, in addition to the electron density profile, data from other physical, chemical, and compositional measurements on the membranes and their constituents.

Determination of an accurate electron density profile is limited by several factors. Phasing of the less intense regions of the lamellar diffraction may be difficult or ambiguous. Several recent papers have discussed the phase problem and direct methods of phasing (Lesslauer and Blasie, 1972; Worthington et al., 1973; Pape, 1974; Moody, 1974). Often, better resolution would distinguish between several possible interpretations of an electron density profile. Higher resolution data is being acquired for several membrane systems (Cain, 1974 *a*, *b*; Cain and Blasie, in preparation; Santillan and Blasie, in preparation). Disorder within and between layers creates continuous as opposed to discrete diffraction, making the integration of the diffraction into discrete reflections required for a conventional Fourier series analysis difficult and/or meaningless.

If there is a distribution in the placement of unit cells, a multilayer will lack long-range order; this is termed lattice disorder. If the electron density profile of each unit cell is not identical, the multilayer is said to exhibit substitution disorder. If the substitution disorder is independent of the lattice disorder, i.e., the electron density profile of each unit cell is independent of its position in the lattice, the total diffracted intensity may be readily described. It consists of a coherent part composed of relatively sharp maxima arising from the lattice of the average unit cell structures superimposed on a relatively smooth incoherent part which arises from fluctuations in the structure of unit cells from their average.

In this paper several approaches[1] are presented to directly obtain the electron den-

[1] The approach in this paper uses Fourier transforms and convolution integrals. The reader may refer to the book by Bracewell (1965) for mathematical details. The books by Hosemann and Bagchi (1962) and Guinier (1963) also have treatments of the mathematics and diffraction theory used in this paper.

sity profile of the average unit cell in a disordered multilayer from the corrected lamellar diffraction and to ascertain the degree of lattice and substitution disorder. Our methods differ considerably from the conventional Fourier series methods used to analyze diffraction from oriented multilayers.

The methods developed here are applied to the lamellar diffraction, at 25 Å resolution, from frog retinal rod outer segments in whole electrophysiologically active retina. The retinal rod data show significant effects due to lattice and substitution disorder, both of which can be quantitatively explained. Other workers have either ignored or poorly approximated the very significant disorder effects (Worthington, 1974, 1973*b*; Blaurock and Wilkins, 1972, 1969; Blaurock, 1972; Corless, 1972; Gras and Worthington, 1969). As such, the electron density profile that we derive is the most accurate to date at this resolution.

GENERAL PROPERTIES OF DIFFRACTION FROM A FINITE DISORDERED MULTILAYER

The total lamellar diffracted intensity is termed $I(s)$, where $s(\text{Å}^{-1}) = 2\sin\theta/\lambda$ is the reciprocal space coordinate. As is shown in Appendix A, $I(s)$, the total intensity, is the sum of a coherent part, $I_c(s)$ (also known as the sampled diffraction), and an incoherent part, $I_i(s)$ (also known as the diffuse scattering). The general diffraction formula, as derived in Appendix A (Eq. 23) is:

$$\begin{aligned} I(s) &= N[\overline{|F_o(s)|^2} - |\bar{F}_o(s)|^2] + (1/d)|\bar{F}_o(s)|^2 \cdot [Z(s) * |\Sigma(s)|^2] \\ &= I_i(s) \qquad\qquad + I_c(s) \end{aligned} \tag{1}$$

where $*$ denotes convolution, $|\ |$ denotes the modulus of a complex number, and $\bar{\ }$ denotes the averaging of a function over all the unit cells in the multilayer. N is the number of unit cells in the multilayer, $F_o(s)$ is the unit cell structure factor or Fourier transform of a unit cell electron density profile, d is the average unit cell nearest neighbor separation in the multilayer, $Z(s)$ is the sampling or interference function, and $\Sigma(s)$ is the shape factor. Eq. 1 is appropriate if the lattice disorder of a finite multilayer is independent of the substitution disorder, i.e. the electron density profile of each unit cell does not depend on its position in the lattice.

Fig. 1 shows plots for all real, autocorrelation, and reciprocal space functions used in this paper, both for a single unit cell and a single element within a unit cell, in a lattice without substitution disorder. The schematic electron density profile shown in Fig. 1 *b* is meant to be typical of a unit cell consisting of two back-to-back "bilayer" membranes. Figs. 2, 5, and 6 are based on this schematic profile. The caption of Fig. 1 also details the conventions used in all the plots in this paper. The reader may wish to look through the first six figures in order to gain a visual feel for the functions discussed in this section. They are specifically referred to later in the text.

The structure factor, $F_o(s)$ (Fig. 1 *d*), is a slowly varying function of s, while the sampling function, $Z(s)$, is sharply peaked at $s = h/d$ (where h is the reflection index). For a multilayer with lattice disorder, $Z(s)$ is less sharply peaked with in-

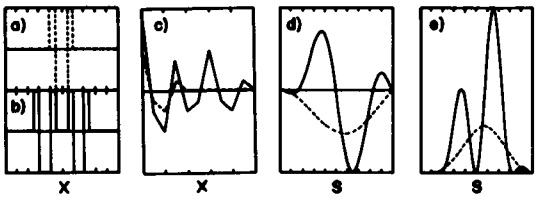

FIGURE 1

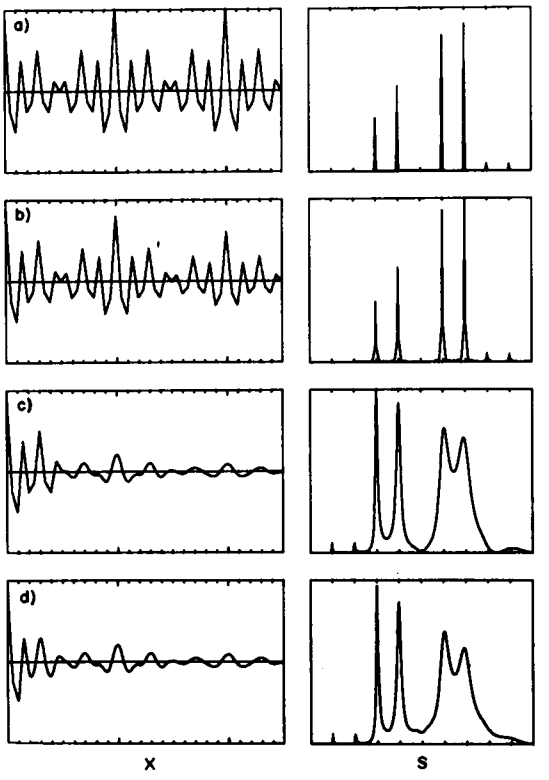

FIGURE 2

CONVENTIONS FOLLOWED FOR ALL FIGURES All real and autocorrelation functions have tick marks at intervals of $0.1d$ and double size tick marks at intervals of d along x. All reciprocal space functions have tick marks at intervals of $1/d$ along s. All superimposed functions are plotted on the same vertical scale. If no mention is made the vertical scale is arbitrary. All autocorrelation functions and reciprocal space functions are only plotted for positive values of x or s as they are all symmetric. The horizontal center line of all electron density profiles is the average electron density, which is set to zero. The horizontal center line on all autocorrelation functions represents zero correlation. Numbers on figures refer to the phase choices listed in Fig. 9. Horizontal axes are labeled x for real and autocorrelation functions and s for reciprocal space functions.

FIGURE 1 Functions associated with a single unit cell (———) and with an element within the unit cell (- - - -). (*a*) $\sigma(x)$, single element electron density profile. (b) $\rho_o(x)$, the unit cell electron density profile, consists of two $\sigma(x)$ at a spacing of $0.3d$. The form of $\rho_o(x)$ is meant to illustrate typical properties of diffraction from a symmetric pair of "bilayer" membranes. (*c*) $\tilde{\sigma}^2(x)$, single element autocorrelation function and $\tilde{\rho}_o^2(x)$, unit cell autocorrelation function. Expressions for $\tilde{\sigma}^2(x)$ and $\tilde{\rho}_o^2(x)$ are Eqs. 29 B and 30 in Appendix B, respectively. (*d*) $F_m(s)$, the single element structure factor, and $F_o(s)$ the unit cell structure factor. (*e*) $|F_m(s)|^2$ and $|F_o(s)|^2$. $|F_o(s)|^2$ is Eq. 33 in Appendix B. $|F_m(s)|^2$ is the transform of $\tilde{\sigma}^2(x)$ and $|F_o(s)|^2$ is the transform of $\tilde{\rho}_o^2(x)$.

FIGURE 2 The Q-function, $Q(x)$, and intensity, $I(s)$, for several types of lattices with the schematic electron density profile, $\rho_o(x)$, of Fig. 1 *b* as the unit cell. Q-functions are in the left column and intensities are in the right. (*a*) An effectively infinite multilayer with an ideal lattice. Peaks in $I(s)$ were arbitrarily drawn as Gaussians of $1/e$ width $1/40d$ and plotted on a vertical scale 4,000× that of Fig. 2 *c*. (*b*) A finite (five unit cells) multilayer with an ideal lattice. (*c*) An effectively infinite multilayer with a disordered lattice ($\gamma/d = 0.067$). (*d*) Same as 2 *c* with the addition of substitution disorder. The relative variation of the center to center interelement distance, $\beta/\bar{a}$, is 0.1. The vertical scale of $I(s)$ is the same as 2 *c*.

creasing s, until it finally becomes constant with an asymptotic value of one (Fig. 3*a*). The coherent intensity is thus the sampling function modulating the slowly varying structure factor modulus squared (Fig. 2*a*, *b*, *c*).

When the shape factor modulus squared, $|\Sigma(s)|^2$, is convoluted into the sampling function, $Z(s)$, the resulting effective sampling function is broadened at each reflection (Fig. 2*b*). $|\Sigma(s)|^2$ becomes narrower as the number of layers in the multilayer increases, until for an infinite multilayer it becomes delta function-like and thus does not broaden $Z(s)$.

The incoherent intensity, $I_i(s)$, is the fluctuation of the structure factor with respect to a distribution of unit cell electron density profiles. $I_i(s)$ is a slowly varying function of s (Fig. 5). It is seen as a slowly varying background underlying the coherent intensity (Fig. 2*d*). If the unit cell consists of two back-to-back mirror image elements, with a varying inter-element distance throughout the multilayer, $I_i(s)$ becomes proportional to the square of the modulus of the single element structure factor at large s. If each unit cell is identical, i.e., there is no substitution disorder, $I_i(s) = 0$ for all s.

The Fourier transform of the total intensity, $I(s)$, is $Q(x)$, the Q-function or generalized Patterson function. $Q(x)$ is the autocorrelation function of the multilayer, with each unit cell being replaced by an average unit cell, plus a fluctuation term. In Appendix A (Eq. 22) it is shown that:

$$Q(x) = N[\tilde{\bar{\rho}}_o^2(x) - \tilde{\bar{\rho}}_o^2(x)] + (1/d)\tilde{\bar{\rho}}_o^2(x) * [z(x) \cdot \tilde{s}^2(x)], \tag{2}$$

where a tilde squared ($\tilde{}^2$) over a symbol denotes the autocorrelation function, also known as the convolution square $[A(x) * A(-x) \equiv \tilde{A}^2(x)]$, i.e. the convolution of a function with its mirror image. $\rho_o(x)$ is the unit cell electron density profile, and $z(x)$ is the lattice autocorrelation function. The autocorrelation function of the average unit cell, $\tilde{\bar{\rho}}_o^2(x)$, may be written as $Q_o(x)$.

The lattice autocorrelation function, $z(x)$, represents the distribution of lattice vector differences in the multilayer. Thus $z(x)$ has a delta function at the origin and peaks at intervals of d from the origin (Fig. 3*b*). If lattice disorder is present, $z(x)$ becomes pseudoperiodic since the peaks in $z(x)$ become increasingly broad and eventually overlap, until at large vector differences $z(x)$ is constant with an asymptotic value of $1/d$. In general, the average unit cell electron density profile, $\bar{\rho}_o(x)$, has an extension of d and therefore its convolution square, $Q_o(x)$, has an extension of $2d$. Convolution of $Q_o(x)$ into $z(x)$ places a $Q_o(x)$ at each value of x weighted by the amplitude of $z(x)$ (Fig. 2). All autocorrelation functions, regardless of the symmetry of their original functions, are centrosymmetric.

The shape function $s(x)$ represents the size of the multilayer. For a multilayer lattice of size Nd, the shape function is unity from $-Nd/2$ to $+Nd/2$ and is zero elsewhere. Its autocorrelation function, $\tilde{s}^2(x)$, has an amplitude of Nd at the origin, and linearly decreases to zero at $\pm Nd$ (Fig. 2*b*). For an effectively infinite multilayer, $\tilde{s}^2(x)$ is constant with an amplitude of Nd, and infinite in extent.

The first term in $Q(x)$, $N[\bar{\tilde{\rho}}_o^2(x) - \tilde{\bar{\rho}}_o^2(x)]$, represents the Fourier transform of the fluctuation of the unit cell structure factor. It exists essentially within $|x| < d$ about the origin, and when added to the second term results in $Q(x)$ about the origin being the average of the unit cell autocorrelation function, $\bar{\tilde{\rho}}_o^2(x)$.

Thus, $Q(x)$, the generalized Patterson function, is pseudoperiodic in d, sharp about the origin, and broadened at large lattice distance differences due to the lattice autocorrelation function, $z(x)$. The properties of $Q(x)$ in the neighborhood of the origin are influenced by the presence of substitution disorder. When lattice disorder is negligible the Q-function decreases linearly in amplitude for a finite multilayer due to multiplication of $z(x)$ by $\tilde{s}^2(x)$ (Fig. 2*b*), the convolution square of the shape function. Otherwise, $Q(x)$ decreases nonlinearly due to the properties of $z(x)$ superimposed on those of $\tilde{s}^2(x)$.

THE COHERENT INTENSITY

If all unit cells are identical, the Q-function and coherent intensity for the multilayer may be derived from the unit cell electron density profile, $\rho_o(x)$, the lattice function, $l(x)$, and the shape function, $s(x)$. The electron density profile of a finite lattice, $\rho(x)$, is:

$$\begin{aligned}\rho(x) &= \rho_o(x) * [l(x) \cdot s(x)] \\ &= \rho_\infty(x) \cdot s(x),\end{aligned} \tag{3}$$

where $\rho_\infty(x)$ is the electron density profile of an infinite lattice. The infinitely extended lattice function, $l(x)$, distributes $\rho_o(x)$ to build up $\rho_\infty(x)$, which when multiplied by $s(x)$ yields $\rho(x)$, the electron density profile of the finite lattice.

After being configurationally averaged to take into account the finite lattice (see Appendix A), the autocorrelation function of $\rho(x)$, $\tilde{\rho}^2(x)$, is the second term of Eq. 2 for $Q(x)$, where $\bar{\rho}_o(x) = \rho_o(x)$, since all unit cells are identical, and the convolution square of the lattice function, $\tilde{l}^2(x)$, is denoted by $z(x)$. The transform of $\tilde{\rho}^2(x)$ is $I_c(s)$, the coherent intensity, where $\bar{F}_o(s) = F_o(s)$ in Eq. 1 for the total intensity, $I(s)$. The substitution disorder term is zero.

For an infinite perfect lattice (with no disorder) $s(x)$ is unity and, $\tilde{s}^2(x)$ is Nd for all x. Both $l(x)$ and its convolution square, $z(x)$, are an infinite linear array of delta functions of weight one, spaced at the lattice repeat distance d. The Fourier transform of $z(x)$ is $Z(s)$, the sampling function, which is also an array of delta functions, of weight $1/d$, with spacing $1/d$ in reciprocal space. Fig. 2*a* shows $Q(x)$ and $I(s)$ for an ideal multilayer.

If the lattice is finite then $s(x)$ is zero outside $\pm Nd/2$. Its convolution square, $\tilde{s}^2(x)$, multiplies $z(x)$ and therefore $Q(x)$ cannot have an extension of greater than $\pm Nd$. The transform of $\tilde{s}^2(x)$, the shape factor modulus squared $|\Sigma(s)|^2$ is:

$$|\Sigma(s)|^2 = (Nd)^2 \operatorname{sinc}^2(\pi s Nd), \tag{4}$$

where $\mathrm{sinc}(\mu) = \sin(\mu)/\mu$. The shape factor modulus squared has an integral width,[2] ϵ, of $1/Nd$. For a perfect but finite multilayer $|\Sigma(s)|^2$ determines the width of the reflections. Fig. 2 *b* shows $Q(x)$ and $I(s)$ for a finite perfect multilayer with five unit cells. Notice that even for this small multilayer the intensity is concentrated in discrete reflections.

For a multilayer with lattice disorder, the lattice autocorrelation function becomes pseudoperiodic and has the form:

$$z(x) = \delta(x) + \sum_{n=1}^{\infty} h_n(x) + \sum_{n=1}^{\infty} h_n(-x), \tag{5}$$

where $h_1(x)$ is the probability that the nearest neighbor unit cell at positive x, is located at a distance x from the unit cell at the origin. The centroid of $h_1(x)$ is at d, the average lattice repeat distance. The probability that the second nearest neighbor is located at x is $h_2(x)$, which is the convolution of $h_1(x)$ with itself, i.e., $h_1(x) * h_1(x)$, with centroid at $2d$. The probability that the nth nearest neighbor is located at x is $h_n(x)$, with centroid at nd, representing $(n-1)$ convolutions of $h_1(x)$ into itself. The delta function represents the fact that each unit cell is located 0 Å from itself. All the $h_n(x)$ are normalized.

The widths of functions increase under convolution; thus if the nearest neighbor distance has a distribution width, γ, the nth nearest neighbor has a distribution width $\sqrt{n}\gamma$ (Fig. 3 *b*). At larger distances the nth neighbor location becomes so diffuse that the peaks in $z(x)$ overlap; finally, $z(x)$ becomes a constant with a value of $1/d$.

The transform of the lattice autocorrelation function, $z(x)$, is the sampling function, $Z(s)$. The sampling function can be shown (Guinier, 1963) to be given by:

$$Z(s) = \{1 - |H(s)|^2\}/[1 + |H(s)|^2 - 2|H(s)|\cos(2\pi ds)], \tag{6}$$

for $|H(s)| \leq 1$ where $|H(s)|$ is the modulus of the transform of $h_1(\pm x)$. If $h_1(x)$ is a Gaussian, then $h_1(\pm x) = (1/\sqrt{\pi}\gamma)\exp(-(x \mp d)^2/\gamma^2)$, where γ is the $1/e$ width and $|H(s)| = \exp(-\pi^2 s^2 \gamma^2)$. The peaks of $Z(s)$ have an area of $1/d$. As s increases the peaks decrease in amplitude and broaden. Finally at large s, $Z(s)$ is constant with an amplitude of unity (Fig. 3 *a*). The approximate integral width, Δs, of the hth peak of $Z(s)$ located at $s = h/d$ is (for low values of h):

$$\Delta s = (\pi^2 h^2/2)(\gamma/d)^2(1/d). \tag{7}$$

Thus, the peak width increases as the square of the reflection index and fractional disorder, γ/d. Fig. 3 shows $z(x)$ and $Z(s)$ for several values of the fractional disorder, γ/d. Fig. 2 *c* shows $Q(x)$ and $I(s)$ for $\gamma/d = 0.067$ and the unit cell in Fig. 1 *b*. Chap-

[2] The integral width, ϵ, of a function $f(x)$ is $\epsilon = \int f(x)\,dx/[f(0)]$, which is the width of a rectangle of equal area and of equivalent height at the origin. The transform of $f(x)$ has an integral width of $1/\epsilon$. Chapter 8 in Bracewell (1965) discusses this and related topics.

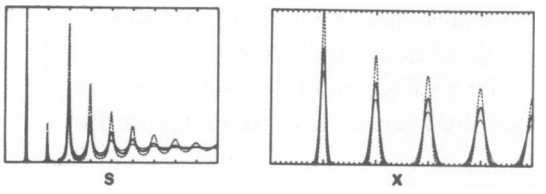

FIGURE 3

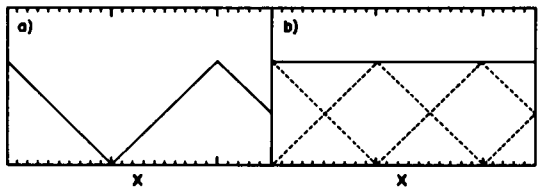

FIGURE 4

FIGURE 3 $Z(s)$ and $z(x)$ for three values of γ/d. (*a*) $Z(s)$, the sampling function. The vertical scale 8× from $2.5/d$ to $10/d$. (*b*) $z(x)$, the lattice autocorrelation function; (- - - -), $\gamma/d = 0.05$; (——), $\gamma/d = 0.067$; (· · · ·), $\gamma/d = 0.083$. $\delta(x)$ at the origin of $z(x)$ and $1/d\ \delta(s)$ at the origin of $Z(s)$ are not shown.

FIGURE 4 The transform of $|F_o(s)|^2$ sampled at a rate of $n/2d$ and n/d. These plots are based on a $\rho_o(x)$ constant from $-d/2$ to $+d/2$. Hence $Q_o(x) \propto d - |x|$ for $|x| < d$. (*a*) $n/2d$. $Q_o(x)$ is recovered in "$Q(x)$" with no overlapping from adjacent $Q_o(x)$'s. (b) n/d. In this case the Patterson function, $P(x)$ is identical to $Q(x)$. The observed $Q(x)$ is denoted by (——), while the component unit cell autocorrelation functions are denoted by (- - - -).

ter 9 of Guinier (1963) has a discussion of lattice disorder and presents derivations of $z(x)$ and $Z(s)$.

Conventional treatments of diffraction often make use of the Patterson function, denoted by $P(x)$. The Patterson function is the autocorrelation function of an infinite perfect crystal constructed by Fourier series summation. Thus for a perfect crystal, $Z(s)$, the sampling function samples the structure factor modulus squared, $|F_o(s)|^2$, only at $s = h/d$ and the transform of this intensity is the Q-function for a perfect crystal. In this case, the Q-function is identical with the conventional Patterson function, because the Fourier sampling theorem identifies the value of the transform of a function sampled at h/d with the corresponding Fourier series coefficients of that function lattiçed to be periodic in d (see Chapter 10 of Bracewell, 1965). Thus we may write the Patterson function as a conventional Fourier series:

$$P(x) = 2 \sum_{h=1}^{m} a_h \cos(2\pi xh/d) + a_o, \tag{8}$$

where $a_h = (1/d)|F_o(s)|^2 \cdot \delta(s - h/d)$ and $\cos(2\pi xm/d)$ is the highest frequency term in the synthesis.

Recall that in general, the electron density profile has an extension of d, and its autocorrelation function, $Q_o(x)$ has an extension of $2d$. Therefore, the Fourier sampling theorem dictates that the transform of $Q_o(x)$, $|F_o(s)|^2$, must be sampled at a minimum frequency of $1/2d$ in order to recover, after transforming, $Q_o(x)$ about the origin undistorted by adjacent overlapping $Q_o(x \pm d)$. Fig. 4 shows the results of sampling the structure factor modulus squared at a frequency of $1/d$ vs. $1/2d$.

If $\rho(x)$ is periodic in d, but the unit cell electron density profile $\rho_o(x)$ has an extension of $\pm d/2$ or less, the Patterson function about the origin will be identical to the unit cell autocorrelation function, $Q_o(x)$. In this case, $Q_o(x)$ has an extension of d (it

is zero from d to $2d$) and will not overlap with itself when latticed to be periodic in d. Fig. 2 *a* illustrates this case for a $\rho_o(x)$ of extension $d/2$.

THE INCOHERENT INTENSITY

In Appendix B we derive an expression (Eq. 38) for the incoherent intensity, $I_i(s) = N(\overline{|F_o(s)|^2} - |\overline{F_o}(s)|^2)$, for an infinite lattice having a unit cell consisting of two mirror-image elements whose separation, a, can vary. The variation in a is assumed to be given by a normalized Gaussian probability function of $1/e$ width β. The variation among the unit cells is uncorrelated with their position in the lattice.

$$\begin{aligned} I_i(s) = N\{&2\cdot[1 - \exp(-\pi^2 s^2\beta^2/2)]\cdot[F_s^2(s) + F_a^2(s)] \\ &+ 2\cdot[\exp(-\pi^2 s^2\beta^2) - \exp(-\pi^2 s^2\beta^2/2)]\cdot[\cos(2\pi\bar{a}s)\cdot(F_s^2(s) - F_a^2(s)) \\ &- 2\cdot F_s(s)\cdot F_a(s)\cdot\sin(2\pi\bar{a}s)]\} \end{aligned} \tag{9}$$

where $\bar{a}$ is the average element-element separation in the multi-layer, β is the $1/e$ width of the Gaussian probability for the element-element separations, $F_s(s)$ is the transform of the symmetric part of an element profile, and $-iF_a(s)$ is the transform of the antisymmetric part of an element profile. The Gaussians in Eq. 9 cause $I_i(s)$ to approach zero at low values of s and $N\{2\cdot[F_s^2(s) + F_a^2(s)]\}$ at high values of s, i.e. N times twice the structure factor modulus squared of a single element. Fig. 5 shows the incoherent intensity calculated for several values of β for the unit cell in Fig. 1 *b*. Fig. 2 *d* shows $I(s)$ for the $\rho_o(x)$ of Fig. 1 *b* and $\beta/\bar{a} = 0.1$.

Separate expressions for $\overline{|F_o(s)|^2}$, $|\overline{F_o}(s)|^2$, and $|F_o(s)|^2$ (Eqs. 36, 31, 33) are given in Appendix B. The transform of Eq. 9 (Eq. 37), which is the first term of $Q(x)$ in Eq. 2 is:

$$\begin{aligned} N[\bar{\tilde{\rho}}_o^2(x) - \bar{\tilde{\rho}}_o^2(x)] = N\{&[1 - (\sqrt{2}/\sqrt{\pi}\beta)\exp(-2x^2/\beta^2)] * [2\cdot\tilde{\sigma}^2(x)] \\ &+ [(1/\sqrt{\pi}\beta)\exp(-x^2/\beta^2) - (\sqrt{2}/\sqrt{\pi}\beta)\exp(-2x^2/\beta^2)] \\ &* [\sigma(x) * \sigma(x) * \delta(x - \bar{a}) + \sigma(-x) * \sigma(-x) * \delta(x + \bar{a})]\} \end{aligned} \tag{10}$$

where $\sigma(x)$ is the single element electron density profile.

The substitution disorder term only affects the Q-function in the region about the origin. It consists of the self-convolutions of $\sigma(x)$ and its mirror image at $+\bar{a}$ and $-\bar{a}$, respectively, and the convolution square of $\sigma(x)$ at the origin, all with appropriate weightings. Consequently, the incoherent intensity is a slowly varying function of s, without any sampling by the relatively sharp interference function (Fig. 5).

As shown in Appendix B (Eq. 30), the convolution square of the unit cell electron density profile, $\tilde{\rho}_o^2(x)$, consists of the single element convolution square placed about the origin and the self-convolutions of the single element and its mirror image placed about $+a$ and $-a$, respectively. The average convolution square of the unit cell electron density profile (Eq. 34), $\bar{\tilde{\rho}}_o^2(x)$, contains only the self-convolutions at $\pm\bar{a}$ convo-

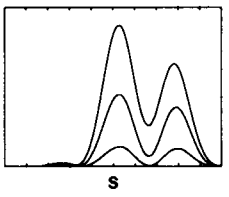

FIGURE 5

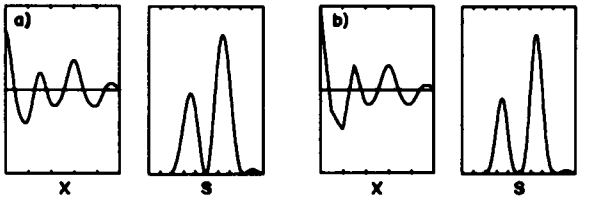

FIGURE 6

FIGURE 5 The incoherent intensity, $I_i(s)$. These plots are based on the $\rho_o(x)$ in Fig. 1 *b*. The lowest curve is for $\beta/\bar{a} = 0.05$ the middle for $\beta/\bar{a} = 0.1$, and the upper for $\beta/\bar{a} = 0.15$. The vertical scale is 6× that of the intensity in Fig. 2 *d*.

FIGURE 6 Unit cell autocorrelation functions and their transforms in the presence of substitution disorder. These plots are based on the $\rho_o(x)$ in Fig. 1 *b*. (*a*) $\tilde{\bar{\rho}}_o^2(x)$, the autocorrelation function of the average unit cell electron density profile and $|\bar{F}_o(s)|^2$, the average structure factor modulus squared for $\beta/\bar{a} = 0.1$. (*b*) $\bar{\tilde{\rho}}_o^2(x)$, the average autocorrelation function of the unit cell electron density profile and $\overline{|F_o(s)|^2}$, the average of the structure factor modulus squared for $\beta/\bar{a} = 0.1$. Plots are on the same scale as corresponding plots in Fig. 1.

luted into a normalized Gaussian of width β, but is unbroadened at the origin. By contrast, the convolution square of the average unit cell electron density profile (Eq. 29), $\tilde{\bar{\rho}}_o^2(x)$, consists of $\tilde{\rho}_o^2(x)$ convoluted into a normalized Gaussian of width $\beta/\sqrt{2}$. Fig. 6 shows $\tilde{\bar{\rho}}_o^2(x)$, $|\bar{F}_o(s)|^2$ and $\bar{\tilde{\rho}}_o^2(x)$, $\overline{|F_o(s)|^2}$ for $\beta/\bar{a} = 0.1$ using the $\rho_o(x)$ shown in Fig. 1 *b*.

The $\bar{\tilde{\rho}}_o^2(x)$ in the substitution disorder term of Eq. 2 for the Q-function cancels the $\tilde{\bar{\rho}}_o^2(x) * \delta(x)$ in the lattice term and therefore $Q(x)$ is $N\bar{\tilde{\rho}}_o^2(x)$, about the origin. In this case, if the extension, w, of an element is $\bar{a}/2$ or less, $Q(x)$ will have the single element convolution square, $\tilde{\sigma}^2(x)$, at the origin, undistorted by lattice or substitution disorder, or by terms at $\pm\bar{a}$. In order for the $Q_o(x)$ contributions at $\pm d$ not to overlap $\tilde{\sigma}^2(x)$ about the origin, $\rho_o(x)$ must be zero or constant outside of $\pm(d - w)/2$.

THE DETERMINATION OF ELECTRON DENSITY PROFILES FROM THE COHERENT INTENSITY

In the previous sections, the properties of lamellar diffraction from a multilayer with lattice and substitution disorder were developed. In this section, we consider the problem of determining the electron density profile and the degree of lattice disorder from the coherent intensity. For this discussion we assume appropriate geometric and camera background corrections have been made to the data. The present discussion is confined to multilayers of infinite extent with symmetric unit cells. In the next section, the problem of separating the total intensity into coherent and incoherent parts is discussed.

Direct Deconvolution Method

The coherent intensity, $I_c(s)$ equals $|\bar{F}_o(s)|^2 \cdot Z(s)$; hence $|\bar{F}_o(s)|^2$ is $I_c(s)/Z(s)$. The sampling function, $Z(s)$, is never quite zero and thus $|\bar{F}_o(s)|^2$ obtained by this method is, in principle, defined for all s.

The sampling function $Z(s)$ is calculated according to Eq. 6 for trial values of the fractional disorder, γ/d. The trial $Z(s)$ is divided into $I_c(s)$ giving a trial $|\bar{F}_o(s)|^2$. The correct $|\bar{F}_o(s)|^2$ is readily recognized since it varies more slowly as a function of s than $I_c(s)$ due to the removal of $Z(s)$. Furthermore, when transformed, the trial $|\bar{F}_o(s)|^2$ yields the average unit cell autocorrelation function $Q_o(x)$ and a proper $Q_o(x)$ *must be zero* outside $\pm d$, while $Q(x)$ is not. Hence, for the correct value of γ/d, division of $I_c(s)$ by $Z(s)$ will result in an unsampled $|\bar{F}_o(s)|^2$ and a $Q_o(x)$ that is most nearly zero outside $\pm d$.

Division of the experimental coherent intensity by a calculated sampling function can give rise to spurious large terms at low-angle because of the camera line width and shape, with which the intensity is convoluted. For the lower orders $Z(s)$ can be narrow compared to typical camera line widths even for $\gamma/d = 0.1$, and thus the camera line shape and width may dominate at lower orders. Hence, the trial $Z(s)$ will be very small on either side of the low-order peaks in $I_c(s)$, giving rise to large spurious terms in the trial $|\bar{F}_o(s)|^2$. One could either convolute the camera line shape into $Z(s)$ or deconvolute it out of $I_c(s)$ to eliminate this effect. In our specific case (section on Analysis of a Set of Data) the lower orders are small, and they were eliminated from $|\bar{F}_o(s)|^2$ before transforming to obtain $Q_o(x)$. Hence, this $Q_o(x)$ cannot be used to distinguish phases for the lower orders.

The $Q_o(x)$ so obtained can be subjected to recursive square root deconvolution to obtain $\rho_o(x)$. The direct deconvolution method is diagrammed in Fig. 7. In this procedure, $Q_o(x)$ is digitized at $4n + 1$ points spaced at $\Delta x = d/2n$ with $Q_o(j)$ being the value of $Q_o(x)$ at $x = j\Delta x$. The interval size is chosen such that $Q_o(x)$ is effectively constant over one interval. The integral equation for $Q_o(x)$ becomes:

$$Q_o(j) = \sum_{i=-n}^{+n} \rho_o(i) \cdot \rho_o(i - j) \qquad -2n \leq j \leq +2n. \tag{11}$$

Eq. 11 is then inverted in order to solve for $\rho_o(x)$. With no additional information Eq. 11 can only be uniquely inverted for a symmetric or antisymmetric $\rho_o(x)$. The uniqueness of this deconvolution is discussed in Chapters IV and XV of Hosemann and Bagchi (1962). Several recent papers have also discussed this method (Lesslauer and Blasie, 1972; Lesslauer et al., 1971; Worthington et al., 1973; McIntosh and Worthington, 1974).

If $\rho_o(x)$ is symmetric, $Q_o(x)$ will in general have an extension of $2d$ being zero for $|x| > d$. If $\rho_o(x)$ consists of a structure surrounded by a fluid medium which is essentially an electron density continuum at the resolution available, $Q_o(x)$ will be effectively constant or zero for $|x|$ greater than this structure width. In either case, if d or the structure width is termed $4k\Delta x$, the sum in Eq. 11 extends from $-k$ to $+k$ and the starting point for the inversion from which all the other values of $\rho_o(x)$ are calculated is $x = 2k\Delta x$ where $\rho_o(k) = \sqrt{Q_o(2k)}$.

At $x = (2k - 1)\Delta x$, $\rho_o(k - 1) = [Q_o(2k - 1)]/2\rho_o(k)$; at $x = (2k - 2)\Delta x$,

$\rho_o(k-2) = [Q_o(2k-2) - \rho_o^2(k-1)]/2\rho(k)$; and at $x = (2k-3)\Delta x$, $\rho_o(k-3) = [Q_o(2k-3) - 2\rho_o(k-1)\rho_o(k-2)]/2\rho_o(k)$.

The general term at $x = (2k-m)\Delta x$ is:

$$\rho_o(k-m) = [Q_o(2k-m) - \sum_{i=1}^{m-1} \rho_o(k-i)\cdot\rho_o(k-m+i)]/2\rho_o(k). \quad (12)$$

Recursive square root deconvolution is a relatively inaccurate procedure because the errors in the initial values of $\rho_o(x)$ are propagated to all the latter values. Also calculating a $\rho_o(k-m)$ involves the differences of large numbers. In practice, the starting point and the interval Δx are varied until the most symmetric solution for $\rho_o(x)$ is obtained. The advantage of the method is that the general features of the unit cell electron density profile will be unambiguously and uniquely defined. Thus, after this procedure, the analysis can then concentrate on phasing the less intense regions of the coherent intensity. An alternative method for the deconvolution of the DDM[3] $Q_o(x)$ which avoids the problem inherent in the recursion method is presented in a different context in the following section.

Generalized Fourier Synthesis Deconvolution Method

The method previously described is straightforward in the sense that $z(x)$ is directly deconvoluted from $Q(x)$ leaving $Q_o(x)$. The unit cell electron density profile, $\rho_o(x)$, is the square root deconvolution of $Q_o(x)$. We can also obtain $\rho_o(x)$ by transforming the square root of the coherent intensity with the addition of phase information. Recall that $Q(x)(I_i(s) = 0)$ is pseudoperiodic in d, with $Q_o(x)$ placed at the origin undistorted by lattice disorder. Similarly, the generalized Fourier synthesis $\rho_-(x)$, termed $\rho'_\infty(x)$, is pseudoperiodic in d due to $l'(x)$, the square root deconvolution of $z(x)$, the lattice autocorrelation function. The lattice function, $l(x)$, which builds the structure from $\rho_o(x)$ (Eq. 3) is *not* pseudoperiodic in d since $l(x)$ is a sum of displaced delta functions representing a lattice (possibly disordered) "frozen" in one configuration. However, $z(x)$ and hence its convolution square root $l'(x)$, the average lattice function, are pseudoperiodic. Note that both $l(x)$ and $l'(x)$ have $z(x)$ as their autocorrelation function. See Appendix A for further details. The delta function at the origin in $l'(x)$ causes $\rho'_\infty(x)$ at the origin to be $\rho_o(x)$ "essentially undistorted" by lattice disorder (Cain, 1974*a*, *b*).

The phased square root of the coherent intensity is:

$$F_o(s)\cdot\sqrt{Z(s)} = \Phi(s)\sqrt{I_c(s)}, \quad (13)$$

where $\Phi(s)$ is either ± 1 in a given region of s when $\rho_o(x)$ is symmetric. The transform of Eq. 13 is the generalized Fourier synthesis:

[3] Abbreviations used are: DDM, direct deconvolution method; GFSDM, generalized Fourier synthesis deconvolution method.

$$\rho_o(x) * l'(x) = \rho'_\infty(x), \tag{14}$$

where $l'(x)$, the average lattice function, is the square root deconvolution of $z(x)$. Thus, $\rho_o(x)$ can be determined by transforming the correctly phased square root of the coherent intensity.

A region of $I_c(s)$ may be zero to experimental accuracy. As such, it might be a place where $F_o(s)$ changes sign. However, $F_o(s)$ or $Z(s)$ may simply have very small amplitude at this point. We thus have a set of apparent zeroes in $I_c(s)$, only some of which are points where the phase changes. Thus, there are 2^m possible phase choices where m is the number of regions of constant phase. Half of these phase choices are pairs with opposite sets of phases and hence have $\rho_o(x)$ and $-\rho_o(x)$ as their transforms.

$\rho'_\infty(x)$ may be calculated for each phase choice. We obtain $\rho_o(x)$ to a good approximation by multiplying $\rho'_\infty(x)$ by a window function that is unity between $-d/2$ and $+d/2$ and zero elsewhere. Transforming $\rho_o(x)$ we obtain $F_o(s)$, whose modulus squared is $|F_o(s)|^2$. Transforming $|F_o(s)|^2$ we obtain $Q_o(x)$. In obtaining $Q_o(x)$ by the DDM in the last section, the fractional disorder, γ/d, was estimated. Hence $Z(s)$ may be calculated. The $|F_o(s)|^2$ is multiplied by $Z(s)$ yielding $I_c(s)$. Transforming $I_c(s)$ we obtain $Q(x)$. These operations are schematically illustrated in Fig. 7.

We can determine $I_c(s)$ and its transform $Q(x)$ from experiment. From the GFSDM we have obtained $I_c(s)$ and $Q(x)$ for each of the possible phase choices. The correct phase choice will have the least deviation from the experimentally determined coherent intensity and Q-function, because $Q_o(x)$, $Q(x)$, $|F_o(s)|^2$ and $I_c(s)$ are unique for a particular phase choice (Hosemann and Bagchi, 1962).

The amount of lattice disorder also may be determined by comparing the width of the peak in $Q(x)$ at the origin, with the lower and broader peak at d. Consequently, if the phase choice is relatively fixed, γ/d can be varied until the peak of the GFSDM $Q(x)$ at $x = d$ matches the experimental one.

The GFSDM is advantageous in that the $\rho_o(x)$ calculated is independent of a specific form for the calculated $Z(s)$. $Z(s)$ multiplies the GFSDM $|F_o(s)|^2$, which contains the phase information. Thus, for all phase choices the GFSDM $I_c(s)$ and $Q(x)$ have the same bias due to possible differences between the calculated and experimental $Z(s)$. Further, the $l'(x)$ in the generalized Fourier synthesis (Eq. 14) is the transform of the square root of the experimental $Z(s)$.

The GFSDM is somewhat more laborious than the DDM since the GFSDM function must be compared to the experimental functions for each phase choice. Hence, if the DDM is used to prune the number of possible phase choices, the GFSDM can compare the remaining possible unit cell electron density profiles.

The GFSDM coherent intensity is more sensitive to phase choices than the GFSDM Q-function, because in $Q(x)$ the phase choice for each region of intensity exerts its influence uniformly over the region $|x| < d$ in $Q_o(x)$, while in $I_c(s)$ a given phase choice mainly influences the intensity in that region of reciprocal space. However, this property of $Q(x)$ vs. $I_c(s)$ has another consequence; namely, the specific details of $I_c(s)$ and hence $Z(s)$ are averaged out in $Q(x)$ making a point by point comparison of the

calculated and experimental Q-function meaningful. Due to camera line width effects, noisy data, and small differences between the actual and calculated sampling function, a point by point difference of the coherent intensities is often rendered difficult. Hence, comparison of the GFSDM and experimental Q-functions, and comparing $\rho_o(x)$ from the GFSDM to the $\rho_o(x)$ obtained by the DDM can phase the more intense regions of the coherent intensity. Final phase choice for less intense regions of the coherent intensity will usually be done by comparing the calculated and observed coherent intensities. For example, the comparison of the integrated intensities of the lower orders if the extension of $\rho_o(x)$ is less than $\pm d/2$ (as is done in this paper in the section on Analysis of a Set of Data), or the comparison of the amplitudes of $|F_o(s)|^2$ obtained from the DDM to the $|F_o(s)|^2$ calculated from the GFSDM may fix that choice.

Each situation will require the investigator to use one, both, or a hybrid of the above approaches to obtain the best electron density profile.

REMOVAL OF INCOHERENT INTENSITY AND STRUCTURE ANALYSIS IN PRACTICE

The previous section dealt with obtaining the electron density profile from the coherent intensity. A real set of data will probably show effects from both lattice and substitution disorder. This is particularly true when the unit cell contains a flattened membrane vesicle, i.e. it is unlikely each vesicle will have an identical gap between its membrane pair. In this section, the problem of dividing the intensity into a coherent and incoherent part is discussed for the case of a relatively small incoherent part.

Fig. 2 *d* shows $Q(x)$ and $I(s)$ for a multilayer with lattice and substitution disorder. Notice that the points where the coherent intensity changes phase (Fig. 1 *d* and Fig. 2 *c*) are now not at zero due to the addition of an incoherent part.

A good beginning for the analysis is to apply the DDM to the total intensity. This is, of course, not rigorously correct as the incoherent intensity should not be divided by $Z(s)$. The approximate $\bar{\rho}_o(x)$ derived can be transformed to help locate the points in $\bar{F}_o(s)$ where the phase changes. These phase change points may then be used as a starting point for the GFSDM. Furthermore, comparison of the electron density profiles obtained by the two methods facilitates appropriate choice of phases for the GFSDM, since the phase choices close to the correct one give rise to a $\bar{\rho}_o(x)$ which is similar to that obtained by the DDM.

Non-zero minima in $I(s)$ could be minima in $|\bar{F}_o(s)|^2$ and/or $Z(s)$, or phase change points raised above the background by $I_i(s)$. The DDM in specifying the fractional disorder, γ/d, may enable some of the minima in $I(s)$ to be assigned to sampling by $Z(s)$ or alternatively to be ruled out as caused by $Z(s)$.

We can specify all the points where the phase might change by knowing $Z(s)$ and the DDM $\bar{\rho}_o(x)$. As such, the GFSDM may be applied. If the incoherent intensity is relatively small, we allow the phase to change at points that are not zero, even though this would rigorously mean that the unit cell structure factor had discontinuities in it.

At this stage, before subtraction of the incoherent intensity, the comparison of the GFSDM vs. experimental Q-function is inappropriate. As pointed out in the section on the incoherent intensity, the Q-function about the origin, in the case where there is substitution disorder, is $\bar{\tilde{\rho}}_o^2(x)$, the unit cell autocorrelation function average. Phase combinations with more regions of identical phase could fit the experimental Q-function better than other phase combinations which break up the incoherent part into regions of different phase. At this point, therefore, the emphasis should be on obtaining an approximate $\bar{\rho}_o(x)$ with which to calculate the incoherent intensity to be subtracted from the total intensity.

The approximate $\bar{\rho}_o(x)$ might be the $\bar{\rho}_o(x)$ from the DDM or the $\bar{\rho}_o(x)$ for one of the phase choices of the GFSDM. Here we treat the case where the medium electron density matches the average unit cell electron density. Hence, the unit cell is considered to consist of only two membranes at an average separation $\bar{a}$ between their centers of electron density. One of these $\sigma(x)$ is considered to be the $\sigma(x)$ in Eq. 10. Single membrane structures derived in this manner are only approximately the $\sigma(x)$ in Eq. 10. Because of finite resolution, $\bar{\rho}_o(x)$ is convoluted with $2s_o \operatorname{sinc}(2\pi x s_o)$, where s_o is the maximum value of s at which $I(s)$ is observed. Due to this effect not only is each $\sigma(x)$ of limited resolution, but its shape has been distorted by the finite electron density around it. Only for relatively poor resolution and small $\bar{a}$ will this effect be important in the calculation of the incoherent intensity.

The single membrane structure can be separated into its symmetric, $\sigma_s(x)$, and antisymmetric, $\sigma_a(x)$, components. Then the incoherent intensity can be calculated according to Eq. 9 for a given value of β, the $1/e$ width of the Gaussian probability for the membrane pair spacing, $\bar{a}$. In order to scale the incoherent intensity for a given value of β to the experimental total intensity, $|F_o(s)|^2$ is calculated from the transform of $\rho_o(x) = [\sigma(x) * \delta(x - \bar{a}/2) + \sigma(-x) * \delta(x + \bar{a}/2)]$. The experimental intensity is scaled[4] to have the same area as this $|F_o(s)|^2$. The experimental intensity and calculated incoherent intensity as a function of β are then plotted on the same scale. The correct value of β is chosen by requiring the calculated incoherent intensity to fill in minima in the experimental intensity that are thought to be phase change points.

Once the incoherent intensity has been separated from the coherent intensity, the GFSDM can be applied to the coherent intensity. Phase choices may be made by comparing GFSDM vs. experimental Q-functions and coherent intensities. The best profile at this stage may be used to calculate a refined incoherent intensity. Because $|\overline{F_o(s)}|^2 =$

[4] We wish to prove $\int |F_o(s)|^2 \, ds = (1/N) \int I(s) \, ds$. For an infinite disordered multilayer $I(s) = N\{|\overline{F_o(s)}|^2 - |\overline{F_o(s)}|^2] + |\overline{F_o(s)}|^2 \cdot Z(s)\}$. Transforming $I(s)$ we obtain $Q(x)$. Thus $\int I(s) \, ds = Q(0)$ and $Q(0) = N\bar{\tilde{\rho}}^2(0)$. From Appendix B we have $\bar{\tilde{\rho}}_o^2(0) = 2\bar{\tilde{\sigma}}^2(0)$ (Eq. 35). Now $\int |F_o(s)|^2 \, ds = \bar{\rho}_o^2(0)$. From Appendix B we also have $\bar{\rho}_o^2(0) = 2\bar{\tilde{\sigma}}^2(0)$ (Eq. 30). Therefore, $\int |F_o(s)|^2 \, ds = (1/N) \int I(s) \, ds$. Hence, when the area of the experimental intensity is set equal to this $|F_o(s)|^2$, the intensity is really $I(s)/N$, the intensity per unit cell. The incoherent intensity calculated on this same scale is $I_i(s)/N = [\overline{|F_o(s)|^2} - |\overline{F_o(s)}|^2]$, and only varying β is needed to fit it to the experimental intensity. The accuracy of this procedure is limited to the accuracy with which the reconstructed $|F_o(s)|^2$ matches the experimental $|F_o(s)|^2$.

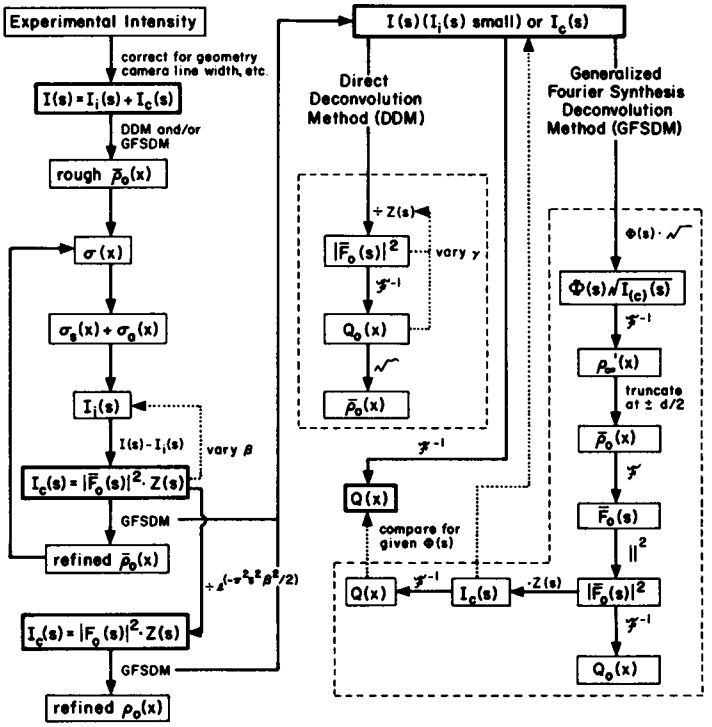

FIGURE 7 Methodology used to obtain unit cell electron density profiles. The left column illustrates the recursive nature of the removal of the incoherent intensity, $I_i(s)$, which involves recalculation of $\bar{\rho}_o(x)$ or $\rho_o(x)$ at each step by the DDM and/or GFSDM, shown in the center and right hand columns, respectively. $\mathfrak{F}$ denotes Fourier transformation; $\mathfrak{F}^{-1}$ denotes inverse Fourier transformation; $\sqrt{}$, denotes square root deconvolution; other symbols defined in the text. A heavy line around a function (——) denotes it a function derived from experiment to be compared to its counterpart calculated by the GFSDM. A dotted line (· · · ·) indicates comparison of calculated vs. experimental functions and/or variation of a parameter. A dashed line (- - - -) is placed around the operations belonging to the DDM and GFSDM. A typical path through the figure would start at the upper left and continue down to the "refined $\bar{\rho}_o(x)$." In this circuit all possible phase choices would be run through the GFSDM. From this $\bar{\rho}_o(x)$ a $\sigma(x)$ could be calculated which would allow $I_i(s)$ to be calculated and subtracted from $I(s)$ leaving $I_c(s)$. The GFSDM could be run through with fewer phase choices at this point. The phase choices would be pared down by comparing the GFSDM and DDM $\bar{\rho}_o(x)$. At this point (or after another circuit or two) only one or two phase choices would remain. Each new refined $\bar{\rho}_o(x)$ will result in the calculations better approximating the actual experimental $I_i(s)$. $I_c(s)$ is then put through the GFSDM with substitution disorder averaging removed resulting in a "refined $\rho_o(x)$." Comparisons made at this stage are between GFSDM and experimental $I_c(s)$ and $Q(x)$ are to the limit of this particular treatment.

$\exp(-\pi^2 s^2 \beta^2/2) \cdot |F_o(s)|^2$ (Eq. 32), division of the coherent intensity by the Gaussian factor will remove the broadening of $\rho_o(x)$ caused by substitution disorder.

The coherent intensity is now determined to the limit of this method. Final phase choices can be made on the GFSDM $\rho_o(x)$'s derived from this coherent intensity. The methods discussed in this section are diagrammed in Fig. 7. It should be stressed that each experimental problem may require some modification of these specific methods.

ANALYSIS OF A SET OF DATA

In the previous two sections, the general approach to obtain the electron density profile and the lattice and substitution disorder for an oriented multilayer was discussed. In this section the method is applied to lamellar diffraction data from dark adapted, elec-

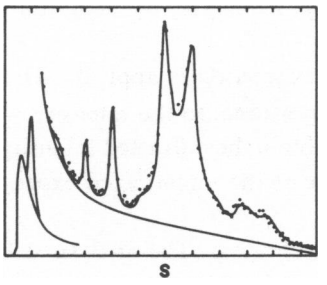

FIGURE 8

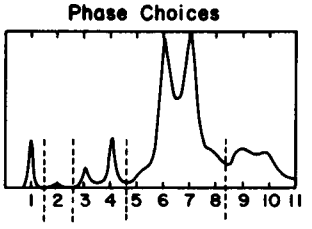

No.	Φ(s)					Step 1	2	3	4
1	+	+	+	+	+	X			
2	+	−	+	+	+	X			
3	+	+	−	+	+	X			
4	+	−	−	+	+	X			
5	+	+	+	−	+	X	X	X	
6	+	−	+	−	+	X	X	X	X
7	+	+	−	−	+	X	X		
8	+	−	−	−	+	X	X		
9	−	−	−	−	+	X	X		
10	−	+	−	−	+	X	X		
11	−	−	+	−	+	X	X	X	
12	−	+	+	−	+	X	X	X	
13	−	−	−	+	+	X			
14	−	+	−	+	+	X			
15	−	−	+	+	+	X			
16	−	+	+	+	+	X			

FIGURE 9

FIGURE 8 Experimental intensity. The filled circles (•) represent channel counts with the full vertical scale being 2,000 counts, except for the first order which is drawn $\frac{1}{8}$ scale. Channel counts are shown for the 2nd through 11th orders. Counting time was 300 s. The line through the filled circles is the continuous intensity which was digitized 18 points/($\Delta s = 1/d$). A curve representing the camera background is drawn beneath the continuous intensity. In this plot the Lorentz correction has not been applied. The data was processed from a continuous curve provided by Chabre before the channel counts were obtained. The fit is not perfect in several places—future work will correct this deficiency.

FIGURE 9 Experimental intensity with possible phase choices. The total intensity is the difference between the experimental intensity and the camera background and is corrected for experimental geometry. The intensity is divided into five regions of constant phase, denoted by dashed lines, resulting in 32 phase choices, 16 of which are inverted versions of their counterparts. These 16 $\Phi(s)$ are enumerated in the figure and denoted by 1 to 16. At the right of the figure are four columns denoting the steps applied to the experimental intensity in order to obtain the best unit cell electron density profile. In each column (x) denotes the remaining phase choices used in that step. Note that the phase change points between the fourth and fifth and seventh and eighth orders are above zero due to the incoherent intensity (shown in Fig. 17).

trophysiologically active rods in *Rana esculanta* retina obtained by Marc Chabre and Andrea Cavaggioni (unpublished). See Chabre and Cavaggioni (1973) for experimental details. The data was obtained using a position sensitive detector and is displayed as number of counts vs. channel number. There are about 13 channels per reflection. A smooth line was drawn through the channel counts to represent the continuous diffracted intensity. Fig. 8 shows the data and background correction. A smooth background was drawn giving zero intensity between the first and second and second and third orders, and a small intensity at the "11th" order.

From the counter to sample distance Chabre and Cavaggioni determined d to be 295 Å ± 3 Å. Hence the distance in our plot of the data between the plus and minus first orders was $s = 2/295$ Å^{-1}. The data was digitized every 0.000188 Å^{-1}. This array of digitized data represents the total lamellar diffracted intensity. The scaling of the reciprocal coordinate is confirmed by the pseudoperiodicity (d = 295 Å) of the Q-function (Fig. 10).

After subtracting the camera background, the Lorentz correction is applied. This corrects the actual experimental intensity so that it is proportional to the intensity of Eq. 1. For the experimental diffraction geometry used to obtain the diffracted intensity of Fig. 8, the appropriate correction multiplies each point of the uncorrected experimental intensity by its reciprocal space coordinate.

Fig. 9 shows the total intensity with the possible phase choices. The analysis will first be discussed in brief outline and then in detail.

In step 1 the total intensity was subjected to the DDM establishing γ/d and the rough unit cell electron density profile. From considerations of the degree of lattice disorder and the expected phase change points for a membrane pair of the spacing found, five possible regions of different phase were determined. The electron density profiles for the 16 possible phase choices were calculated by the GFSDM. Only eight had any possible resemblance to the $\bar{\rho}_o(x)$ from the DDM.

In step 2 the $\bar{\rho}_o(x)$ of phase choice five was used to calculate an incoherent intensity which was subtracted from the total intensity leaving the coherent intensity. The

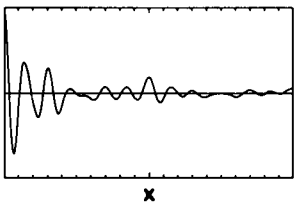

FIGURE 10

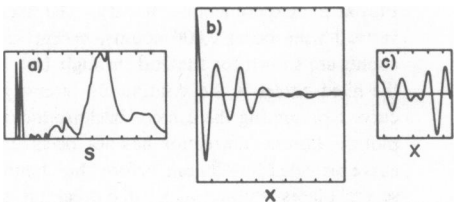

FIGURE 11

FIGURE 10 The experimental Q-function of step 1. This Q-function is the transform of the intensity in Fig. 9.

FIGURE 11 The results of the DDM at step 1. (*a*) $|\bar{F}_o(s)|^2$; (*b*) $Q_o(x)$; (*c*) $\bar{\rho}_o(x)$. The sharp peaks about the first and second orders were truncated before transforming to obtain $Q_o(x)$. The square root deconvolution started at 145 Å and $Q_o(x)$ was digitized every 2.95 Å. A smaller digitization interval did not change the results.

DDM was reapplied to the coherent intensity, giving a more symmetric $\bar{\rho}_o(x)$. Electron density profiles were calculated by the GFSDM for the eight phase choices, only four of which resembled the $\bar{\rho}_o(x)$ from the DDM.

In step 3 the new profile for the fifth phase choice was used to compute a refined incoherent intensity. The GFSDM was applied to these four remaining phase choices. The fifth and sixth phase choices were selected on the basis of their matches to the experimental Q-function. The sixth choice was then chosen on the basis of its match to the experimental intensity.

In step 4 the profile for the sixth phase choice was used to recompute the incoherent intensity. After the Gaussian of substitution disorder had been divided out of the coherent intensity the GFSDM was reapplied. The calculated refinements were quantitatively close to the previous iteration.

Step 1

The experimental Q-function is shown in Fig. 10. As both the coherent and incoherent intensity were transformed, $Q(x)$ has $\bar{\bar{\rho}}_o^2(x)$ about the origin. Fig. 11 shows $|\bar{F}_o(s)|^2$, $Q_o(x)$, and $\bar{\rho}_o(x)$ obtained by the DDM for $\gamma = 20$ Å.

At this stage, points between the first and second orders, (0.00546 Å^{-1}), second and third orders (0.00904 Å^{-1}), fourth and fifth orders (0.0156 Å^{-1}), and eighth and ninth orders (0.0268 Å^{-1}) were chosen as possible phase change points. The points on either side of the second order are zero to our experimental accuracy because $Z(s)$ for $\gamma = 20$ Å is quite small in this region. They could additionally be zero because $\bar{F}_o(s)$ is small or changes phase. The latter two phase change points were chosen because they closely correspond to the phase change points of $\cos(\pi 88s)$ which modulates the single membrane transform, $F_s(s)$, in the transform of a pair of symmetric membranes at 88 Å spacing. The last phase change point is at too sharp a minimum to be caused by $Z(s)$; hence it can only be a true phase change point elevated by the incoherent intensity, a minimum in $|\bar{F}_o(s)|^2$, or a minimum in $|\bar{F}_o(s)|^2$ elevated by the incoherent intensity.

All the 16 possible electron density profiles were calculated by the GFSDM at this stage. They are shown in Fig. 12. Only phase choices 5–12 resemble $\bar{\rho}_o(x)$ obtained by the DDM. Fig. 13 shows $|\bar{F}_o(s)|^2$, $I_c(s)$, $Q_o(x)$, and $Q(x)$ for phase choice 6 calculated by the GFSDM.

Step 2

At this point a single membrane electron density profile was obtained by considering $\bar{\rho}_o(x)$ for phase choice five from 0 to 93Å to be $\sigma(x)$. The membrane pair separation was 88 Å. The incoherent intensity was calculated for several values of β, the variation in the spacing of the membranes within the membrane pair. For each value of β, the incoherent intensity was scaled to the experimental intensity as described in the previous section. The incoherent intensity for $\beta = 9$ Å and $\bar{a} = 88$ Å, filled in the minima at 0.0156 Å^{-1} and 0.0268 Å^{-1}, and was subtracted from the to-

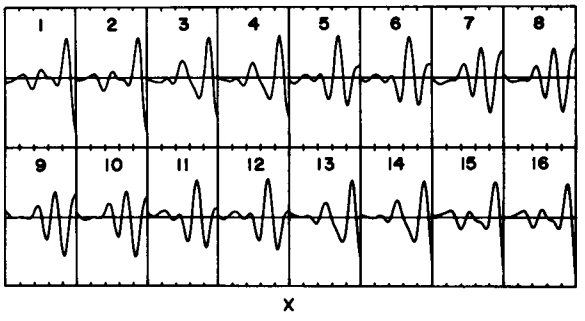

FIGURE 12

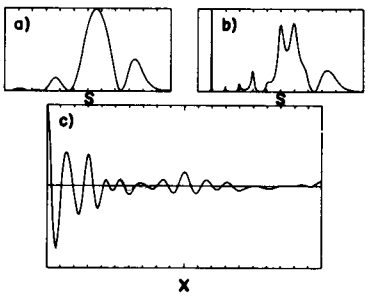

FIGURE 13

FIGURE 12 The sixteen $\bar{\rho}_o(x)$ from GFSDM applied at step 1. The symmetric $\rho_o(x)$ are shown from 0 to $d/2$. The area of the total experimental intensity is fixed and all $\bar{\rho}_o(x)$ are plotted with the same vertical scale factor.

FIGURE 13 Functions calculated by the GFSDM for phase choice 6 at step 1. (*a*) $|\bar{F}_o(s)|^2$; (*b*) $I_c(s)$; (*c*) $Q(x)$, (——); $Q_o(x)$, (· · · ·). Notice the oscillations in $Q_o(x)$ and $Q(x)$ in region of $d/2$. Phase choices 5, 11, and 12 also show this property. At this point the incoherent intensity has not been removed from the experimental intensity.

tal intensity. Any points that became slightly negative in the coherent intensity were set to zero before additional calculations were performed.

The coherent intensity was now subjected to the DDM. We expect $Q_o(x)$ to be relatively flat outside of $d/2$ which is approximately the width of the two membranes in the unit cell, and $|F_o(s)|^2$ not to display the sampling evident in $I_c(s)$. By these criteria $\gamma = 19$ Å was chosen as the best estimate of the lattice disorder. Furthermore, the $\bar{\rho}_o(x)$ obtained by square root deconvolution was much more symmetric than that originally obtained from the total intensity. Fig. 14 shows $|\bar{F}_o(s)|^2$, $Q_o(x)$ and $\bar{\rho}_o(x)$ obtained from the DDM at this stage.

The electron density profiles for all eight phase possibilities were calculated by the GFSDM and compared to that from the DDM. Fig. 15 shows these profiles. Only profiles for phase choices 5, 6, 11, and 12 look sufficiently close. The excluded phase choices 7, 8, 9, 10 differ from 5, 6, 11, and 12 in the third phase region, encompassing the third and fourth orders. Fig. 16 shows $|\bar{F}_o(s)|^2$, $I_c(s)$, $Q_o(x)$ and $Q(x)$ for phase choice 6 calculated by the GFSDM.

The remaining four phase choices are the four combinations for the phases in the first and second regions. Their profiles are quite similar, hence, comparisons of GFSDM vs. experimental Q-functions and coherent intensities are necessary.

Step 3

Two comparison indices were devised. Because the intensity is relatively sharp for the first two orders, the integrated intensity for the first two orders was compared for the GFSDM and experimental coherent intensity. This comparison is valid because the extension of $\rho_o(x)$ determined in the preceeding steps is essentially less than $d/2$ and hence, the integrated intensities of the lower orders are unique to $\rho_o(x)$. The experi-

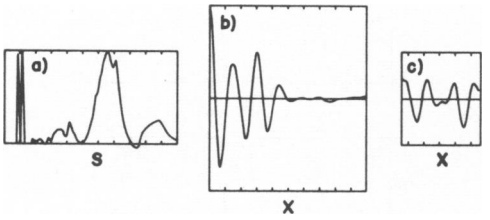

FIGURE 14

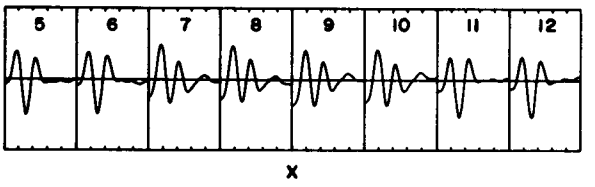

FIGURE 15

FIGURE 14 The results of the DDM at step 2. (*a*) $|\bar{F}_o(s)|^2$; (*b*) $Q_o(x)$; (*c*) $\bar{\rho}_o(x)$. The same procedure was followed as in Fig. 11.

FIGURE 15 The eight $\bar{\rho}_o(x)$ from the GFSDM at step 2. Symmetric $\bar{\rho}_o(x)$ are shown from 0 to $d/2$. The total experimental intensity is scaled to same area as in Fig. 12. The $I_t(s)$ is then subtracted. The $\bar{\rho}_o(x)$ are plotted with the same vertical scale factor as in Fig. 12.

mental coherent intensity and GFSDM coherent intensity were scaled to the same area. The comparison was not done point by point because of camera broadening evident in the experimental intensity. On the other hand, the GFSDM Q-functions could be compared, point by point, to the experimental Q-function because the camera line width is narrow enough not to significantly affect the Q-function within $|x| < 2d$. In addition, the GFSDM Q-functions are not attenuated at large x values by the transform of the camera line shape. Thus, they all have the same bias relative to the experimental Q-function, which is attenuated. The point by point difference of the calculated and experimental Q-functions was squared and integrated from 0 to $d/2$ to provide an agreement index. The integrated areas were normalized by dividing by the width of the integrated region. Inasmuch as the preceding steps have shown that $\rho_o(x)$ has an ex-

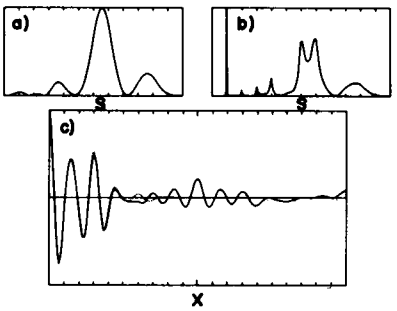

FIGURE 16

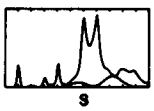

FIGURE 17

FIGURE 16 Functions calculated by the GFSDM for phase choice six at step 2. (*a*) $|\bar{F}_o(s)|^2$; (*b*) $I(s)$; (*c*) $Q(x)$, (——); $Q_o(x)$, (· · · ·). The incoherent intensity has been removed from the experimental intensity using the $\bar{\rho}_o(x)$ from step 1 for phase choice five and $\beta = 9$ Å.

FIGURE 17 The incoherent intensity from step 4 is drawn with the total experimental intensity. The incoherent intensity which is the lower curve, was calculated from the $\bar{\rho}_o(x)$ of step 3 for $\beta = 8$ Å.

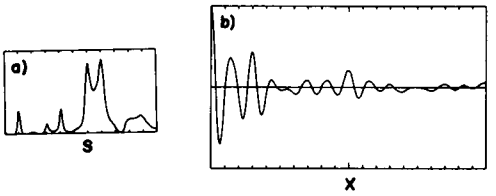

FIGURE 18

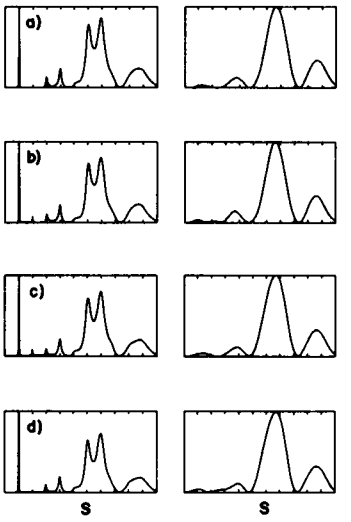

FIGURE 19

FIGURE 18 The experimental $I_c(s)$ and $Q(x)$ at step 4. (*a*) $I_c(s)$; (*b*) $Q(x)$. $I_c(s)$ is the difference between the $I(s)$ and $I_t(s)$ in Fig. 17. $I_c(s)$ is plotted without removal of substitution disorder averaging. All other functions from step 4 are plotted with removal of substitution disorder averaging.

FIGURE 19 $I_c(s)$ and $|F_o(s)|^2$ from the GFSDM at step 4. Phase choices: (*a*) 5; (*b*) 6; (*c*) 11; (*d*) 12. Coherent intensities are in the left columns and structure factor moduli squares in the right. Substitution disorder averaging was removed.

tension essentially of less than $d/2$, the region $0 \leq x \leq d/2$ in $Q(x)$ provides the most reliable test of the possible phase choices.

The incoherent intensity was recalculated for phase combination five at this stage. The incoherent intensity was subtracted for $\beta = 8$ Å. The above mentioned indices were calculated. Phase choices five and six were selected on the basis of the Q-function index and then phase choice six was chosen as most correct on the basis of the intensity index. As the final calculation used phase combination six for the incoherent intensity, giving very similar results, it will be discussed in detail.

Step 4

At this point the incoherent intensity was recalculated for the sixth phase choice. The minima at 0.0156 Å^{-1}, and 0.0268 Å^{-1} were filled in best for $\beta = 8$ Å. Fig. 17 shows the total intensity with the calculated incoherent intensity.

The experimental coherent intensity at this stage is $|\bar{F}_o(s)|^2 \cdot Z(s)$, where $|\bar{F}_o(s)|^2 = |F_o(s)|^2 \cdot \exp(-\pi^2 s^2 \beta^2/2)$. The multiplication by the Gaussian represents the averaging of $\rho_o(x)$ over the variation in membrane pair spacing. By dividing the experimental coherent intensity by the Gaussian, substitution disorder averaging may be removed.

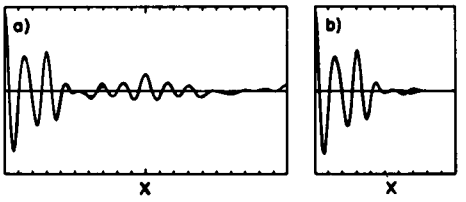

FIGURE 20

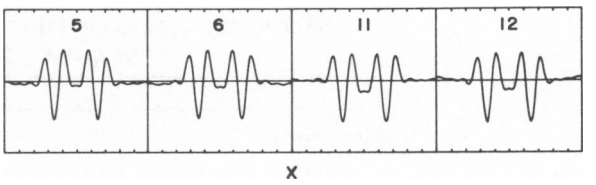

FIGURE 21

FIGURE 20 The GFSDM $Q(x)$ and $Q_o(x)$ at step 4. (*a*) $Q(x)$; (*b*) $Q_o(x)$. Both have had substitution disorder averaging removed. Phase choices: 5 (- - - -), 6 (——), 11 (— —), and 12 (· · · ·).
FIGURE 21 The GFSDM $\rho_o(x)$'s at step 4. The symmetric $\rho_o(x)$ are shown from $-d/2$ to $+d/2$. Phase choice six is the correct structure. The total experimental intensity was set to the same area as in Fig. 12. The $I_i(s)$ is then subtracted and is divided by $\exp(-\pi^2 s^2 \beta^2/2)$ to remove substitution disorder averaging. The vertical scale is the same as Fig. 12.

$I_c(s)$, $Q(x)$, $\tilde{\rho}^2(x)$, $|F_o(s)|^2$, and $\rho_o(x)$ were calculated by the GFSDM for the four remaining phase combinations. Fig. 18 shows experimental $I_c(s)$ and $Q(x)$ for this step. Figs. 19, 20, and 21 show the results of the GFSDM. Table I shows the normalized integrated root mean square deviation of the calculated and experimental Q-function in the region $x = 0$ to $d/2$. The results of this comparison indicate that phase choices five and six are best. Table II compares the normalized areas of the first order, the second order, and their ratio; phase choice six is closest for all three criteria, i.e. the first and second orders are each of the proper intensity.

Several comments are appropriate on the changes seen in the experimental DDM and GFSDM functions as we progress from step 1 to step 4. Recall that in step 1 the experimental intensity did not have the incoherent part removed.

The $\rho_o(x)$ at step 4 (Fig. 21) and the $\bar{\rho}_o(x)$ at step 2 (Fig. 15) are flatter in the extramembrane region than the $\bar{\rho}_o(x)$ at step 1 (Fig. 12) for phase choices 5, 6, 11, and 12. Further, by step 3 $\bar{\rho}_o(x)$ (not shown) and $\rho_o(x)$ at step 4 show a small resolution ripple that was not evident in earlier steps.

At step 1 the experimental $Q(x)$ (Fig. 10), the DDM $Q_o(x)$ (Fig. 11 *b*), and the GFSDM $Q_o(x)$ and $Q(x)$ (Fig. 13 *c*) for phase choice 6 (and 5, 11, and 12) have a higher peak at 42 Å than at 88 Å. This situation is reversed for their counterparts for step 2 onward (see Figs. 18, 14, 16, and 20). Also, the GFSDM $Q_o(x)$ for phase choice

TABLE I
ROOT MEAN SQUARE DIFFERENCE PER Å OF THE GFSDM $Q(x)$ AND THE EXPERIMENTAL $Q(x)$ AT STEP 4

Phase choice	(0 to d/2) × 10^{-2}
5	4.3
6	4.4
11	5.6
12	5.9

Both Q(x) were scaled to height 1 at the origin. Note the average root mean square difference is about three parts in one thousand.

TABLE II

INTEGRATED AREAS OF FIRST AND SECOND ORDERS IN $I_c(s)$ AT STEP 4

	First	Second	Second/first
Experimental	0.030	0.0039	0.13
5(++)	0.026	0.0019	0.073
6(+-)	0.028	0.0039	0.14
11(--)	0.028	0.0047	0.16
12(-+)	0.030	0.0016	0.053

The numbers in the left most column refer to the phase choices in Figure 9 and the two symbols in parentheses refer to the sign of $\Phi(s)$ in the first and second orders, respectively. The entries refer to the fractional area of $I_c(s)$ that is under the first and second orders and their ratio.

6 (and 5, 11, and 12) at step 3 and 4 oscillates much less between $d/2$ and d than at Step 1 or 2.

These progressive changes are due to the progressive refinement of our removal of the incoherent intensity.

We rely primarily on the comparison of the calculated and experimental Q-functions to select the most probable phase choices (five and six) and secondarily on comparing the calculated and experimental intensities in order to resolve the remaining ambiguity for the reason stated earlier, i.e. the effects of the first and second order phase differences are localized near the first and second orders in the coherent intensity but are delocalized in the Q-function.

In summary, the analysis has demonstrated that phase choice six is the best phase choice in the region of reciprocal space $s \leq 1/25$ Å^{-1}. Thus, the correct electron density profile for the disk membrane pair at 25 Å resolution is given in Fig. 21 for phase choice six. The disorder parameters determined by the analysis are $d = 295$ Å, $\gamma = 19$ Å for the lattice disorder and $\bar{a} = 88$ Å, $\beta = 8$ Å for the substitution disorder. There is a range of uncertainty in the shape and amplitude of the camera background that must be subtracted from the data before the analysis. On both this set of data and one of the sets provided by Costello and Corless varying the curvature and amplitude of the camera background within reasonable limits had very small effects on the phasing criteria in real and reciprocal space and the calculated electron density profiles. The lower intensity backgrounds required that a somewhat greater (about 10%) incoherent intensity be subtracted from the total intensity to minimize the amplitude near 0.0156 Å^{-1} and 0.0268 Å^{-1}. This general shape of $I_t(s)$ does not change as β is varied over a wide range (see Fig. 5). Hence, the calculated incoherent intensity is empirically found to largely compensate for different camera backgrounds. And the reasonable range of uncertainty in the background only leads to an uncertainty in the quantitative estimate of the substitution disorder.

DISCUSSION AND CONCLUSIONS

Theoretical Aspects

(*1*) We note that the theoretical approaches described in this paper for the direct analysis of lamellar diffraction from disordered multilayers utilize the uniqueness of the experimental functions $Q(x)$, $Q_o(x)$, $I(s)$ [$I_c(s)$ and $I_i(s)$], and $|F_o(s)|^2$ to their respective calculated functions for the correctly phased unit cell electron density profile $\rho_o(x)$ when $\rho_o(x)$ is centrosymmetric. For the coherent diffraction, this essentially involves the identification of $Q_o(x)$ within $Q(x)$ and $|F_o(s)|^2$ within $I_c(s)$, which becomes possible when the multilayer is simply disordered (see part 2 below) and/or finite. While Hosemann and Bagchi (1962) recognized the utility of this identification for the case of finite crystals, we believe this paper to be the first to utilize this identification for the case of simply disordered multilayers in the direct solution of the unit cell electron density profile. These theoretical approaches followed naturally from our earlier analysis of lamellar diffraction from finite multilayers of model membranes (Lesslauer and Blasie, 1972; Lesslauer et al., 1971).

We also note that the phasing procedure in real space utilizing the functions $Q(x)$ and $Q_o(x)$ is most sensitive to the phases of the more intense regions of $I_c(s)$ in reciprocal space. Conversely, the phasing procedure in reciprocal space utilizing the functions $I_c(s)$ and $|F_o(s)|^2$ is also sensitive to the phases of the less intense regions of $I_c(s)$. As a result, both phasing procedures in real and reciprocal space may be necessary to select the correct phase choice for all s and hence determine the correct unit cell electron density profile $\rho_o(x)$.

(*2*) With regard to a general approach to the phasing of lamellar diffraction from disordered multilayers, one must select a model for the disorder which can completely account for the experimental functions $Q(x)$ and $I(s)$ within experimental errors.

The first level would include only simple lattice disorder. In this case, the phasing procedure is independent of the lattice disorder (including the exact form of the lattice nearest neighbor statistics) and its magnitude. This level of analysis has proved sufficient for isolated retinal receptor disk membrane multilayers (Santillan and Blasie, in preparation), sarcoplasmic reticulum multilayers (Marquardt and Blasie, in preparation), and model lipid and lipid-protein multilayer systems (Blasie et al., 1974; Torriani, Blasie, and Dutton, in preparation).

The second level would include simple lattice disorder and also a form of substitution disorder which was independent of the lattice disorder. In the case of membrane multilayers, substitution disorder can include random membrane fragment sidedness, random membrane vesicle sidedness, and a membrane spacing variation within a membrane pair (Cain, 1974*a*). In such cases, an iteration procedure must be adopted in order to maintain the phasing procedure distinct from the determination of the disorder parameters. This level of analysis has proved sufficient for intact retinal rod disk multilayers (this work) and photosynthetic bacterial chromatophore multilayers (Cain, 1974*a*,*b*; Cain and Blasie, in preparation).

A next logical higher level would include interdependent lattice and substitution

disorders. An example of such disorder would occur when the membrane spacing within a membrane pair were coupled with the local separation of adjacent membrane pairs in the multilayer. We have not yet examined such direct phasing procedures under these circumstances.

In conclusion, it is important to note that in certain conditions of disorder within multilayer systems, the phasing procedure can be made to be independent of the determination of the disorder parameters. In such cases, the phasing procedure can be direct, utilizing the uniqueness properties of the functions $Q(x)$ and $Q_o(x)$ in real space and/or the functions $I_c(s)$ and $|F_o(s)|^2$ in reciprocal space. In addition, the best model for the disorder(s) completely accounts for these experimental functions within experimental errors.

Experimental Aspects

(*1*) We utilized the lamellar diffraction data from dark-adapted retinal rod outer segments obtained with a position sensitive X-ray detector. We have found the data of Chabre and Cavaggioni (unpublished) and that of Costello and Corless (unpublished) to be the most accurate to date with regard to linearity in intensity and position. However, in future experiments, the background should be experimentally determined, since its *precise* form becomes important in the consideration of substitution disorder. It should also be determined that the incoherent (diffuse) scattering has the same degree of orientation as the coherent (sampled diffraction) scattering from the oriented multilayer—otherwise, disordered impurities in the multilayer could give rise to diffuse scattering which could be mistakenly interpreted as arising from substitution disorder in the multilayer lattice. Finally, the Lorentz correction should also be experimentally determined using diffractometer methods (ω-scans) for all regions of reciprocal space utilized in the analysis. These methods have been recently employed in neutron diffraction experiments (Zaccai et al., 1975).

(*2*) We believe that the particular form of substitution disorder, independent of lattice disorder, employed here at 25 Å resolution, i.e., a variation in the separation of the two apposed membranes of the disk among the unit cells of the multilayer, is essentially correct. Not only is it necessary to explain the low-angle lamellar diffraction from retinal rods, but it also predicts the observed higher-angle lamellar diffraction which behaves as the single-membrane structure factor modulus squared (Blaurock and Wilkins, 1969). In addition, the substitution disorder observed in lamellar diffraction from retinal rods in glycerol and sucrose (Costello and Corless, unpublished) is also readily explained by such a form of substitution disorder. Further analysis of this latter data is in progress.

(*3*) Finally, a complete disorder analysis of the lamellar diffraction from retinal rods is necessary in order to obtain the most accurate profile structure for the disk since this profile is to be "modeled" with respect to rhodopsin and lipid structure and location in the membrane. In addition, changes in disorder parameters dominate the structural changes of the retinal rod during rhodopsin bleaching as observed in the lamellar diffraction obtained via position sensitive X-ray detectors (Chabre and Cavag-

gioni, 1973, and unpublished). Hence, these changes in disorder parameters must be determined in order to also determined changes in disk membrane structure which may occur during rhodopsin bleaching. The analyses of such data are in progress.

APPENDIX A

General Diffraction Formula

In this section we calculate the lamellar diffraction arising from a finite one dimensional crystal in which the distribution of lattice spacings is unrelated to the distribution of unit cell electron density profiles. In other words, the structure of a given unit cell is independent of its position in the lattice. The approach used here is to consider a given finite one dimensional crystal and average its autocorrelation function over all possible configurations allowed by the statistical distributions of unit cell structures and lattice spacings. An equivalent approach would be to consider an infinite one dimensional crystal, $\rho_\infty(x)$, "frozen" in a given configuration (which over the infinite crystal is statistically representative of the actual finite crystal) and to sum the autocorrelation functions from an infinite number of finite regions of the size of the actual crystal, each located at a different value of x. Guinier (1963), Chapter 2, uses an approach similar to the one used here, i.e. the diffraction is averaged from a finite crystal. Hosemann and Bagchi (1962), Chapter VI, use the latter approach.

We first consider a finite one dimensional crystal in a given configuration:

$$\rho(x) = \sum_{n=1}^{N} \rho_n(x) * \delta(x - x_n)$$
$$= \sum_{n=1}^{N} \rho_n(x - x_n), \tag{15}$$

where $\rho_n(x - x_n)$ is located at $x = x_n$ and N is the number of unit cells in the crystal. If all the $\rho_n(x)$ are identical, Eq. 15 is another way of writing Eq. 3.

We take the autocorrelation function of Eq. 15, which is termed $Q(x)$,

$$Q(x) = \sum_{n=1}^{N} \rho_n(x) * \delta(x - x_n) * \sum_{k=1}^{N} \rho_k(-x) * \delta(x + x_k)$$
$$= \sum_{n=1}^{N} \sum_{k=1}^{N} \rho_n(x) * \rho_k(-x) * \delta(x - x_n + x_k). \tag{16}$$

We regroup Eq. 16 into terms for $n = k$ ($x = 0$) and terms for $n \neq k$ ($x = x_n - x_k$). This expression is averaged over all possible configurations of the multilayer, denoted by a bar ($\overline{\ }$). By allowing all possible statistically allowed configurations to occur, our $Q(x)$ becomes a proper statistical expectation value and therefore representative of the experimentally obtained Q-function of an actual crystal with disorder (for further discussion, see the last two paragraphs of this Appendix).

We obtain:

$$Q(x) = \sum_{n=1}^{N} \overline{\rho_n^2}(x) * \delta(x) + \sum_{\substack{n=1 \\ n \neq k}}^{N} \sum_{k=1}^{N} \overline{\rho_n(x) * \rho_k(-x) * \delta(x - x_n + x_k)}, \tag{17}$$

where the tilde squared ($\tilde{}^2$) indicates an autocorrelation function, i.e. $\bar{\tilde{\rho}}_n^2(x)$ denotes the average autocorrelation function of the nth unit cell and the bar over $Q(x)$ is suppressed.

We assume that the unit cell electron density profiles are unrelated to their positions in the lattice and only the average properties of the nth unit cell are correlated with the average properties of the kth unit cell. Hence:

$$Q(x) = N\tilde{\bar{\rho}}_o^2(x) * \delta(x) + \tilde{\bar{\rho}}_o^2(x) * \sum_{\substack{n=1 \\ n \neq k}}^{N} \sum_{k=1}^{N} \delta(x - \overline{x_n + x_k}), \tag{18}$$

where $\bar{\rho}_o(\pm x)$ represents the average unit cell electron density profile in the sums replacing $\bar{\rho}_n(x)$ and $\bar{\rho}_k(-x)$, and $\tilde{\bar{\rho}}_o^2(x)$ denotes the autocorrelation function of the average unit cell. Subtracting $N\tilde{\bar{\rho}}_o^2(x) * \delta(x)$ from the first term in Eq. 18 and adding it to the second term we obtain:

$$Q(x) = N[\tilde{\bar{\rho}}_o^2(x) - \tilde{\bar{\rho}}_o^2(x)] + \tilde{\bar{\rho}}_o^2(x) * \sum_{n=1}^{N} \sum_{k=1}^{N} \delta(x - \overline{x_n + x_k}). \tag{19}$$

The double sum for $N \to \infty$ is identified with $Nz(x)$, i.e., N times the normalized autocorrelation function of a statistically averaged lattice. Assuming there is lattice disorder and N large, $z(x)$ is a smoothly varying function except at the origin, where an infinite number of delta functions have been added together. Hence, the infinite sum for $n - k = 1$ represents the statistical distribution of lattice nearest neighbor spacings which is denoted by $h_1(x)$ in the text (similarly for $h_2(x), \ldots h_n(x)$ [Eq. 5]). Thus Eq. 19 may be written for large N as:

$$Q(x) = N[\tilde{\bar{\rho}}_o^2(x) - \tilde{\bar{\rho}}_o^2(x) + \dot{\tilde{\bar{\rho}}}_o^2(x) * z(x)]. \tag{20}$$

Its transform is $I(s)$, the total intensity:

$$I(s) = N[|\overline{F_o(s)}|^2 - |\bar{F}_o(s)|^2 + |\bar{F}_o(s)|^2 \cdot Z(s)], \tag{21}$$

where $F_o(s)$ is the unit cell structure factor, $Z(s)$ is the sampling function, and $|\ |$ denotes the modulus of a function.

For finite N, the derivation of equations analogous to Eq. 20 and 21 is more difficult. We use configuration averaging of the double sum in Eq. 19 to give a statistically averaged $z(x)$. We proceed by identifying the finite double sum with $(1/d)\, z(x) \cdot \tilde{s}^2(x)$; $\tilde{s}^2(x)$ is the convolution square of the shape function and d is the average lattice repeat. The shape function, $s(x)$, is unity from $-Nd/2$ to $+Nd/2$, and zero elsewhere. Its convolution square, $\tilde{s}^2(x)$, is Nd at the origin and linearly decreases to zero at $\pm Nd$. Multiplication of the infinite double sum by $(1/d)\, \tilde{s}^2(x)$ is equivalent to taking the finite double sum with configuration averaging to give a proper statistically averaged and therefore "smooth" $z(x)$. This can be simply demonstrated as follows. For the general term at $x = x_n - x_k$, there are, on the average, $(N - |n - k|)$ terms in the finite double sum (Eq. 19). Since $z(x)$ is normalized, i.e.,

$$z(x) = \lim_{N \to \infty} \frac{1}{N} \sum_{n=1}^{N} \sum_{k=1}^{N} \delta(x - \overline{x_n + x_k}),$$

each peak has the weight of one delta function. Multiplication by $(1/d)\, \tilde{s}^2(x)$ weights $z(x)$ by

$(1/d)(Nd - |x|) = (N - |x|/d)$ for $|x| < Nd$. As $x = x_n - x_k$, $|x|/d \approx |n - k|$. Hence, $z(x)$ weighted by $(1/d)\tilde{s}^2(x)$ at $x = x_n - x_k$ also has $(N - |n - k|)$ terms. Therefore, multiplying $z(x)$ by $(1/d)\tilde{s}^2(x)$ is equivalent to taking the finite double sum in Eq. 19. The bar over $\delta(x - \overline{x_n + x_k})$ ensures a statistically averaged $z(x)$ even for a finite crystal. Without it the double sum for a very small crystal would not be smoothly varying. With averaging we get a proper statistical $z(x)$, averaged over all possible statistically allowed configurations even if N is small. For a disordered infinite crystal the double sum gives an average $z(x)$ without having to rely on configuration averaging because an infinite double sum of displaced delta functions is effectively a continuum and exhibits the proper disorder statistics. It is for this reason that $l(x)$, the lattice function, and $l'(x)$, the average lattice function, both have $z(x)$ as their convolution square (see Eq. 14). For further discussion the reader is referred to Hosemann and Bagchi (1962), Chapters VI and VII. Thus Eq. 19 may be written for finite N as:

$$Q(x) = N\{\bar{\tilde{\rho}}_o^2(x) - \bar{\tilde{\rho}}_o^2(x)\} + (1/d)\,\bar{\tilde{\rho}}_o^2(x) * [z(x) \cdot \tilde{s}^2(x)]. \tag{22}$$

The transform of Eq. 22 is the total intensity:

$$I(s) = N\{\overline{|F_o(s)|^2} - |\bar{F}_o(s)|^2\} + (1/d)|\bar{F}_o(s)|^2 \cdot [Z(s) * |\Sigma(s)|^2], \tag{23}$$

where $\Sigma(s)$ is the shape factor. The first term is the incoherent intensity $I_i(s)$, and the second term is the coherent intensity, $I_c(s)$.

APPENDIX B

Incoherent Intensity Due to Variation in Intra-Unit Cell Membrane Pair Spacing

We consider the unit cell to be composed of two back-to-back mirror-image elements $\sigma(x)$ and $\sigma(-x)$ at spacing a in a medium of zero electron density. The unit cell structure may be represented by:

$$\begin{aligned} \rho_o(x) &= \sigma(x) * \delta(x - a/2) + \sigma(-x) * \delta(x + a/2), \\ \sigma(x) &= \sigma_s(x) + \sigma_a(x);\ F_m(s) = F_s(s) - iF_a(s) \\ \sigma(-x) &= \sigma_s(x) - \sigma_a(x);\ F_m^*(s) = F_s(s) + iF_a(s), \end{aligned} \tag{24}$$

where $\sigma(x)$ is the single element electron density profile whose transform is $F_m(s)$, $\sigma_s(x)$ is the symmetric part of the single element electron density profile whose transform is $F_s(s)$, and $\sigma_a(x)$ is the antisymmetric part of the single element electron density profile whose transform is $-iF_a(s)$.

In Appendix A, the incoherent intensity due to substitution disorder was shown to be $N(\overline{|F_o(s)|^2} - |\bar{F}_o(s)|^2)$, the bar denoting the configuration averaging. In this section, we calculate $\overline{|F_o(s)|^2}$ and $|\bar{F}_o(s)|^2$ for the case where a varies about its mean value $\bar{a}$ as a Gaussian, $g(a)$. Variation in intra-unit cell element spacing is a special case of variation in structure throughout a crystal that configuration averaging takes into account.

The distribution in a is normalized and is written as:

$$g(a) = (1/\sqrt{\pi}\beta)\exp(-(a - \bar{a})^2/\beta^2). \tag{25}$$

Thus,

$$\bar{\rho}_o(x) = \int \rho_o(x) g(a)\, da \tag{26}$$

gives the result of the configuration averaging for this case.

Derivation of $|\bar{F}_o(s)|^2$. Substituting Eq. 24 into Eq. 26 we have:

$$\bar{\rho}_o(x) = \sigma(x) * \int \delta(x - a/2) \cdot (1/\sqrt{\pi}\beta) \exp(-(a - \bar{a})^2/\beta^2)\, da + \sigma(-x) * \int \delta(x + a/2) \cdot (1/\sqrt{\pi}\beta) \exp(-(a - \bar{a})^2/\beta^2)\, da \tag{27 A}$$

The delta functions cause the integrals to be zero except at $x = \pm a/2$.

$$\bar{\rho}_o(x) = \sigma(x) * (2/\sqrt{\pi}\beta) \exp(-(2x - \bar{a})^2/\beta^2) + \sigma(-x) * (2/\sqrt{\pi}\beta) \exp(-(2x + a)^2/\beta^2). \tag{27 B}$$

Extracting the delta functions from the Gaussians we obtain:

$$\bar{\rho}_o(x) = \sigma(x) * (2/\sqrt{\pi}\beta) \exp(-4x^2/\beta^2) * \delta(x - \bar{a}/2) + \sigma(-x) * (2/\sqrt{\pi}\beta) \exp(-4x^2/\beta^2) * \delta(x + \bar{a}/2). \tag{28 A}$$

Thus $\bar{\rho}_o(x)$ is:

$$\bar{\rho}_o(x) = \rho_o(x) * (2/\sqrt{\pi}\beta) \exp(-4x^2/\beta^2). \tag{28 B}$$

We now take the autocorrelation function of $\bar{\rho}_o(x)$ and transform to obtain $|\bar{F}_o(s)|^2$.

$$\bar{\rho}_o(x) * \bar{\rho}_o(-x) = (\sqrt{2}/\sqrt{\pi}\beta) \exp(-2x^2/\beta^2) * \tilde{\rho}_o^2(x), \tag{29}$$

where:

$$\sigma(x) * \sigma(x) = \sigma_s(x) * \sigma_s(x) + 2\sigma_s(x) * \sigma_a(x) + \sigma_a(x) * \sigma_a(x), \tag{29 A}$$

$$\sigma(x) * \sigma(-x) = \sigma_s(x) * \sigma_s(x) - \sigma_a(x) * \sigma_a(x), \tag{29 B}$$

$$\sigma(-x) * \sigma(-x) = \sigma_s(x) * \sigma_s(x) - 2\sigma_s(x) * \sigma_a(x) + \sigma_a(x) * \sigma_a(x), \tag{29 C}$$

and

$$\tilde{\rho}_o^2(x) = \sigma(x) * \sigma(x) * \delta(x - a) + 2\tilde{\sigma}^2(x) + \sigma(-x) * \sigma(-x) * \delta(x + a). \tag{30}$$

Transforming Eq. 29 we obtain:

$$|\bar{F}_o(s)|^2 = \exp(-\pi^2 s^2 \beta^2/2) \cdot \{[F_s^2(s) - 2iF_s(s) \cdot F_a(s) - F_a^2(s)] \cdot \exp(-2\pi i \bar{a} s) + 2F_s^2(s) + 2F_a^2(s) + [F_s^2(s) + 2iF_s(s) \cdot F_a(s) - F_a^2(s)] \cdot \exp(2\pi i \bar{a} s)\}. \tag{31}$$

Upon use of trigonometric identities Eq. 31 may be written as:

$$|\bar{F}_o(s)|^2 = \exp(-\pi^2 s^2 \beta^2/2) \cdot |F_o(s)|^2, \tag{32}$$

where

$$|F_o(s)|^2 = 4F_s^2(s)\cos^2(\pi \bar{a} s) - 8F_s(s)F_a(s)\cos(\pi \bar{a} s)\sin(\pi \bar{a} s) + 4F_a^2(s)\sin^2(\pi \bar{a} s). \tag{33}$$

. *Derivation of* $\overline{|F_o(s)|^2}$. Our approach is to average $\tilde{\rho}_o^2(x)$ (Eq. 30) over the variation in a and then to transform to obtain $\overline{|F_o(s)|^2}$. Therefore, $\bar{\tilde{\rho}}_o^2(x) = \int \tilde{\rho}_o^2(x) g(a)\,da$ is:

$$\begin{aligned}\bar{\tilde{\rho}}_o^2(x) = {} & \sigma(x) * \sigma(x) * \int \delta(x - a) \cdot (1/\sqrt{\pi}\beta)\exp[-(a - \bar{a})^2/\beta^2]\,da \\ & + 2\tilde{\sigma}^2(x) * \int (1/\sqrt{\pi}\beta)\exp(-(a - \bar{a})^2/\beta^2)\,da \\ & + \sigma(-x) * \sigma(-x) * \int \delta(x + a) \cdot (1/\sqrt{\pi}\beta)\exp[-(a - \bar{a})^2/\beta^2]\,da. \end{aligned} \tag{34}$$

The first and third integrals are zero except at $x = \pm a$. The second integral has a value of unity. Thus,

$$\begin{aligned}\bar{\tilde{\rho}}_o^2(x) = {} & 2\tilde{\sigma}^2(x) + (1/\sqrt{\pi}\beta)\exp(-x^2/\beta^2) \\ & * [\sigma(x) * \sigma(x) * \delta(x - \bar{a}) + \sigma(-x) * \sigma(-x) * \delta(x + \bar{a})]. \end{aligned} \tag{35}$$

Transforming Eq. 35 and using trigonometric identities we obtain:

$$\begin{aligned}\overline{|F_o(s)|^2} = {} & 2F_s^2(s)[1 + \exp(-\pi^2 s^2 \beta^2)\cos(2\pi \bar{a} s)] \\ & - 4F_s(s)F_a(s)[\exp(-\pi^2 s^2 \beta^2)\sin(2\pi \bar{a} s)] \\ & + 2F_a^2(s)[1 - \exp(-\pi^2 s^2 \beta^2)\cos(2\pi \bar{a} s)]. \end{aligned} \tag{36}$$

Derivation of $N\{\overline{|F_o(s)|^2} - |\bar{F}_o(s)|^2\} = I_i(s)$. We proceed by taking the difference $\bar{\tilde{\rho}}_o^2(x) - \tilde{\rho}_o^2(x)$ and transforming:

$$\begin{aligned}N[\bar{\tilde{\rho}}_o^2(x) - \tilde{\rho}_o^2(x)] = {} & N\{[1 - (\sqrt{2}/\sqrt{\pi}\beta)\exp(-2x^2/\beta^2)] * [2 \cdot \tilde{\sigma}^2(x)] \\ & + [(1/\sqrt{\pi}\beta)\exp(-x^2/\beta^2) - (\sqrt{2}/\sqrt{\pi}\beta)\exp(-2x^2/\beta^2)] \\ & * [\sigma(x) * \sigma(x) * \delta(x - \bar{a}) + \sigma(-x) * \sigma(-x) * \delta(x + \bar{a})]\}. \end{aligned} \tag{37}$$

Upon transforming and use of trigonometric identities we obtain:

$$\begin{aligned}N[\overline{|F_o(s)|^2} - |\bar{F}_o(s)|^2] = {} & N\{2[1 - \exp(-\pi^2 s^2 \beta^2/2)][F_s^2(s) + F_a^2(s)] \\ & + 2[\exp(-\pi^2 s^2 \beta^2) - \exp(-\pi^2 s^2 \beta^2/2)] \cdot [\cos(2\pi \bar{a} s)(F_s^2(s) \\ & - F_a^2(s)) - 2F_s(s)F_a(s)\sin(2\pi \bar{a} s)]\}. \end{aligned} \tag{38}$$

We wish to thank Marc Chabre, Andrea Cavaggioni, Joe Corless, and Joe Costello for furnishing unpub-

lished data; Doris Heinsohn for her work on the figures; Dotty Hollinger and Nancy Hogan for helping prepare the manuscript; and George Miljanich, Peter Nemes, and Greg Santillan for reading the manuscript.

This work was supported by Public Health Service grants EY 00673 (to J. K. Blasie) and EY 00175 (to E. A. Dratz). S. Schwartz was supported by a Fight for Sight Student Fellowship Award, Fight for Sight, Inc., New York, during part of his work.

Received for publication 5 June 1975.

REFERENCES

BLASIE, J. K., I. TORRIANI, and P. L. DUTTON. 1974. The X-ray structure of photosynthetic reaction center-phospholipid model membranes. *Fed. Proc.* **33**:1253.

BLAUROCK, A. E. 1972. Structure of the retinal membrane containing the visual pigments. *Adv. Exp. Med. Biol.* **24**:53.

BLAUROCK, A. E., and M. H. F. WILKINS. 1969. Structure of frog photoreceptor membranes. *Nature (Lond.).* **223**:906.

BLAUROCK, A. E., and M. H. F. WILKINS. 1972. Structure of retinal photoreceptor membranes. *Nature (Lond.).* **236**:313.

BRACEWELL, R. 1965. The Fourier Transform and Its Applications. McGraw-Hill, Inc., New York.

CAIN, J. E. 1974 *a*. Lattice and substitution disorder in oriented membrane systems: structure of the chromatophore membrane by X-ray diffraction. Ph.D. Thesis, University of Pennsylvania, Philadelphia.

CAIN, J. E. 1974 *b*. The structure of the chromatophore membrane determined by X-ray diffraction. *Fed. Proc.* **33**:1461.

CHABRE, M., and A. CAVAGGIONI. 1973. Light induced changes of ionic flux in the retinal rod. *Nat. New Biol.* **244**:118.

CORLESS, J. M. 1972. Lamellar structure of bleached and unbleached rod photoreceptor membranes. *Nature (Lond.).* **237**:229.

DUPONT, Y., S. C. HARRISON, and W. HASSELBACH. 1973. Molecular organization in the sarcoplasmic reticulum membrane studied by X-ray diffraction. *Nature (Lond.).* **244**:555.

GRAS, W. J., and C. R. WORTHINGTON. 1969. X-ray analysis of retinal photoreceptors. *Proc. Natl. Acad. Sci. U.S.A.* **63**:233.

GUINIER, A. 1963. X-ray diffraction. P. Lorrain and D. S-M. Lorrain, trans. W. H. Freeman and Company, San Francisco, Calif.

HOSEMANN, R., and S. N. BAGCHI. 1962. Direct Analysis of Diffraction by Matter. North-Holland Publishing Company, Amsterdam.

LESSLAUER, W., and J. K. BLASIE. 1972. Direct determination of the structure of barium stearate multilayers by X-ray diffraction. *Biophys. J.* **12**:175.

LESSLAUER, W., J. CAIN, and J. K. BLASIE. 1971. On the location of 1-anilino-8-naphthalene sulfonate (ANS) in lipid model systems: an X-ray diffraction study. *Biochem. Biophys. Acta.* **241**:547.

LEVINE, Y. K. 1973. X-ray diffraction studies of membranes. *Prog. Surf. Membr. Sci.* **3**:279.

LEVINE, Y. K., and M. H. F. WILKINS. 1971. Structure of oriented lipid bilayers. *Nat. New Biol.* **230**:69.

LUZZATI, V. 1968. *In* Biological Membranes. D. Chapman, editor. Academic Press, London.

MCINTOSH, T. J., and C. R. WORTHINGTON. 1974. Direct determination of the lamellar structure of peripheral nerve myelin at low resolution (17 Å). *Biophys. J.* **14**:363.

MOODY, M. F. 1974. Letter to the editor: Structure determination of membranes in swollen lamellar systems. *Biophys. J.* **14**:697.

PAPE, E. H. 1974. X-ray small angle scattering. A new deconvolution method for evaluating electron density distributions from small angle scattering diagrams. *Biophys. J.* **14**:284.

SHIPLEY, G. G. 1973. *In* Biological Membranes. D. Chapman and D. F. H. Wallach, editors. Academic Press, London. **2**:1.

WORTHINGTON, C. R. 1973 *a*. X-ray diffraction studies on biological membranes. *Curr. Top. Bioenerg.* **5**:1.

WORTHINGTON, C. R. 1973 *b*. X-ray analysis of retinal photoreceptor structure. *Exp. Eye Res.* **17**:487.

WORTHINGTON, C. R. 1974. Structure of photoreceptor membranes. *Ann. Rev. Biophys. Bioeng.* **3**:53.

WORTHINGTON, C. R., G. I. KING, and T. J. MCINTOSH. 1973. Direct structure determination of multilayered membrane-type systems which contain fluid layers. *Biophys. J.* **13**:480.

WORTHINGTON, C. R., and S. C. LIU. 1973. Structure of sarcoplasmic reticulum membranes at low resolution (17 Å). *Arch. Biochem. Biophys.* **157**:573.

ZACCAI, G., J. K. BLASIE, and B. P. SCHOENBORN. 1975. Neutron diffraction studies on the location of water in lecithin bilayer model membranes. *Proc. Natl. Acad. Sci. U.S.A.* **72**:376.